Development of a silicon photomultiplier based gamma camera

Development of a silicon photomultiplier based gamma camera

By

Ashley T. Tao, B.Sc.(Hon)

A Thesis

Submitted to the School of Graduate Studies
in Partial Fulfilment of the Requirements
for the Degree

Master of Science

McMaster University

MASTER OF SCIENCE (2011) (Medical Physics)	McMaster University Hamilton, Ontario

TITLE:	Development of a silicon photomultiplier based gamma camera
AUTHOR:	Ashley T. Tao, B.Sc.(Hon)
SUPERVISOR:	Dr. Troy H. Farncombe
NUMBER OF PAGES:	xi, 124

Abstract

Dual modality imaging systems such as SPECT/CT have become commonplace in medical imaging as it aids in diagnosing diseases by combining anatomical images with functional images. We are interested in developing a dual modality imaging system combining SPECT and MR imaging because MR does not require any ionizing radiation to image anatomical structures and it is known to have superior soft tissue contrast to CT. However, one of the fundamental challenges in developing a SPECT/MR system is that traditional gamma cameras with photomultiplier tubes are not compatible within magnetic fields. New development in solid state detectors has led to the silicon photomultiplier (SiPM), which is insensitive to magnetic fields.

We have developed a small area gamma camera with a tileable 4x4 array of SiPM pixels coupled with a CsI(Tl) scintillation crystal. A number of simulated gamma camera geometries were performed using both pixelated and monolithic scintillation crystals. Several event positioning algorithms were also investigated as an alternative to conventional Anger logic positioning. Simulations have shown that we can adequately resolve intrinsic spatial resolution down to 1 mm, even in the presence of noise. Based on the results of these simulations, we have built a prototype SiPM system comprised of 16 detection channels coupled to discrete crystals. A charge sensitive preamplifier, pulse height detection circuit and a digital acquisition system make up our pulse processing components in our gamma camera system. With this system, we can adequately distinguish each crystal element in the array and have obtained an energy resolution of $30 \pm 1\,\%$ (FWHM) with Tc-99m (140 keV). In the presence of a magnetic field, we have seen no spatial distortion of the resultant image and have obtained an energy resolution of $31 \pm 3\,\%$.

This thesis is dedicated to my late mother, Helen Tao who has always supported me in every way possible and knew that I would succeed in anything I pursued. I am indebted to my mom for everything she has done and sacrificed for me to be where I am today.

Acknowledgements

First and foremost, I would like to express my sincere gratitute and appreciation to my supervisor, Troy Farncombe for his guidance, patience and support throughout this project. I would like to thank Soo Hyun Byun and Nicholas Bock for taking the time to be a part of my committee, and their advice and input during the past two years. Thank you to Eric Da Silva for introducing me to LaTeX and assisting with formatting my thesis. I am extremely grateful to my Medical Physics friends who have always been there for me throughout both my undergraduate and graduate years, and have taken the time to contribute to the editing of my thesis. And finally, many thanks to my family and friends for their unconditional love and support. A special thank you to my aunt, Ann Linton for everything she has done for me and for her support through the most difficult time in my life. Without her, I don't think I would have even made it to graduate school.

Contents

List of Figures

List of Tables

One

Preface

The structure of this thesis begins with an introduction to dual modality imaging and a justification for developing a SPECT/MR system. This is followed by an introductory section on background information such as radiation interactions with materials, a brief summary of various types of radiation detectors, the components of a gamma camera, a more in-depth discussion of silicon based solid state photodetectors.

In Chapter 2, there is a literature review of current applications such as low photon counting applications, high energy physics and medical imaging applications. There is further discussion on dual modality imaging, more specifically with SPECT/MR and prospective clinical applications with this imaging system.

In a clinical gamma camera, there are protocols set out by NEMA NU1 to maintain standards on scintigraphic camera performance. Some of these measurements include determining the intrinsic spatial and energy resolution of the system, intrinsic spatial linearity, system uniformity and system sensitivity (NEMA Standards Publication, 2001). We have performed simulations to identify these performance characteristics and we have modified the tests to suit our system to characterize these measurements for our gamma camera. A detailed outline of the simulation and the results are discussed in Chapter 3. Various image reconstruction algorithms were tested with different gamma camera geometries. As well, there is a detailed summary on the components of a gamma camera, including the various types of preamplifiers, peak detection circuits, and analog to digital conversion. The specifications for each detector component in our gamma camera system is discussed.

Chapter 4 summarizes the results of our gamma camera system. We compare the simulations with our reconstructed images. The spectral responses are characterized for radiation sources of various energies, crystal geometries, and bias voltages. Our gamma camera was also characterized within a magnetic field environment and the results were compared to the measurements in the absence of a magnetic field. There is also a discussion of our detector limitations and potential improvements to overcome these limitations.

We then conclude the thesis with a summary of the results of our gamma camera performance characteristics and potential future developments such as expanding to a larger area detector.

Two

Introduction

2.1 Nuclear Medicine Imaging

Nuclear Medicine imaging is a non-invasive imaging technique which uses radioisotopes to image biological processes within the body (Cherry et al., 2003). They are generally labelled with a compound which targets a particular area of pathologic interest. The radioisotope undergoes radioactive decay and emits gamma rays and/or subatomic particles. Gamma rays which exit the body are detected by an external radiation detector to produce an image. While the uptake of some radiotracers may show some anatomical information, it is predominantly used to highlight areas of pathology and biologic processes such as tissue perfusion and glucose metabolism (Cherry et al., 2003).

There are two main types of nuclear medicine imaging, single photon emission computed tomography (SPECT) and positron emission tomography (PET). The fundamental difference between the two is the detection of one gamma ray versus two coincident gamma rays as needed to create an image. In

SPECT, images are acquired from single gamma rays emitted from radiotracers which are incident on gamma cameras whereas PET uses a positron emitting radiotracer. The positron undergoes annihilation with an electron, emitting two 511 keV photons at 180°. Coincident detection (within a specified time window) of the annihilation photons results in a detected event. Planar images are two dimensional projections of the tracer distribution through the body. A cross sectional image of the body is composed of multiple planar images at varying angles called tomographs (Cherry et al., 2003).

Multimodality Imaging

Multimodality imaging has become an indispensible tool in diagnosing diseases, aiding in treatments and surgeries. PET/CT (x-ray computed tomography) and SPECT/CT are the most common multimodality imaging systems and have been widely used for oncology applications. A multimodal system allows one to correlate functional information with anatomical references and it allows for better image registration due to a common patient support, thus making it more convenient and potentially more cost effective to perform image acquisition simultaneously or sequentially (Wagenaar et al., 2006).

While there are many advantages to this technology and the modalities of imaging used, there are some drawbacks to the ones in current clinical use. Patients are exposed to a larger amount of radiation as a result from x-rays and the injected radiotracers. Magnetic resonance imaging (MRI) is an alternative imaging modality to CT which requires no ionizing radiation.

Nuclei in the body that have an odd number of protons possess an intrinsic angular momentum called spin. Hydrogen is the most abundantly used nuclei in MRI imaging, which consists of a single proton. Three major components of MRI hardware include the main magnetic field (1.5-7T), a radio-frequency (RF) pulse and the magnetic field gradients. The main magnetic field is used aligns the nuclei to an equilibrium state. The RF pulse is used to change the local magnetization of the nuclei during image acquisition and the magnetic field gradients are used to provide spatial localization (Buxton, 2009). Besides the benefit of no exposure to ionizing radiation, MR may be superior to other anatomical imaging techniques due to its ability to obtain some functional information and its excellent soft tissue contrast (Wagenaar et al., 2006). There has been significant development in multimodality imaging in the past decade with PET and MR (Hamamura et al., 2010); however, little development of SPECT/MR has been done. Since SPECT imaging has many more applications than PET, it stands to reason that SPECT/MR could have a greater clinical impact. PET is widely used for oncology applications; however, SPECT can be used to for cardiac, brain, renal and bone imaging just to name a few.. Depending on the type of imaging

One of the fundamental challenges in incorporating these modalities is that the gamma camera is not operable in a magnetic field (Buzhan et al., 2001; SensL, 2010e). Gamma cameras consist of a scintillator coupled to a photomultiplier tube (PMT). Inside the photomultiplier tube, electrons are accelerated across voltage potentials to generate a signal. In the presence of a magnetic field, the trajectory of the electron would be altered, thus distorting the signal. As a result, we are investigating a new type of semiconductor detector, silicon photomultipliers which have been reported to be insensitive to magnetic fields as an alternative to photomultiplier tubes. Provided the magnetic field from MRI doesn't affect the performance of silicon photomultipliers and the accompanying electronics, SiPM based gamma cameras may become the new standard in SPECT imaging.

2.2 Radiation Interactions

The discussion of interactions of radiation with matter is important before delving into the physics of detecting radiation. Photon interaction with a material can occur in one of several ways which include: i) the photoelectric effect, ii) Compton scattering and iii) pair production. Depending on the energy of the photons, there is an associated probability that it will undergo a particular interaction represented by the cross section. At lower energies and high Z materials, the probability of the photoelectric effect dominates, whereas Compton scattering will more likely occur at higher energies and lower Z materials. Pair production will only occur if the photon energy exceeds 1.022 MeV (the sum of the rest mass of an electron and it's antiparticle, the positron). In nuclear medicine we are generally interested in relatively lower energy photons, so pair production isn't a significant interaction. However, it should be noted that some radiotracers in nuclear medicine do emit high energy gamma rays in which case, pair production would be relevant. The following is a brief description of the relevant interactions.

Photoelectric Effect

When a gamma ray of sufficient energy (greater than or equal to that of the binding energy of the electron) is absorbed by the atom, a bound electron is ejected from the atom. The ejected electron has energy equal to the difference between the binding energy of the electron shell and the incident photon. Since photoelectric absorption increases with the strength of electron binding, photons are generally ejected from the K shell (Wernick and Aarsvold, 2004). Photons with energy below the K-shell binding energy will go on to interact with electrons in the L and M shell.

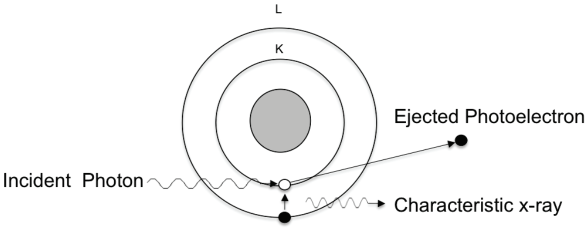

Figure 2.1: Photoelectric Effect

A vacancy exists from where the electron was ejected. To stabilize the atom, an electron from an outer shell will fill the hole while emitting a characteristic x-ray with energy equal to the difference between the two energy levels (Ahmed, 2007). In low Z materials, the characteristic x-ray energy is on the order of a few keV, whereas in high Z material the energy could be on the order of 20-100 keV (Cherry et al., 2003). Therefore, for interactions occurring within the body, energy from these x-rays are generally negligible. For high Z materials, the x-rays may contribute to background. Additionally, the characteristic x ray may go on to eject an electron from an outer shell provided the energy is equal to the binding energy of the electron. The release of this electron is known as an Auger electron and since the photon is absorbed in the Auger electron, radiation is not emitted (Ahmed, 2007).

$$\sigma \propto \frac{Z^n}{E^3} \tag{2.1}$$

The probability of photoelectric interaction is represented by the approximative cross section in eqn. 2.1 where n is between 4 and 5 (Ahmed, 2007). Therefore as the atomic number increases, the probability of the photoelectric effect interaction occurring increases significantly. However, as the energy approaches the rest mass of an electron, the Compton interaction dominates as shown in fig. 2.2 (Cherry et al., 2003).

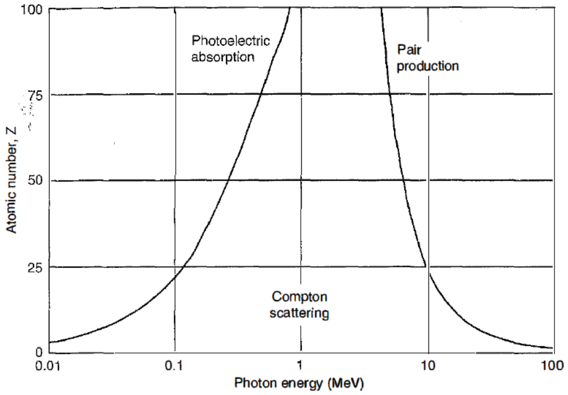

Figure 2.2: Interaction probability of atomic number Z versus photon energy

Compton Scattering

Compton scattering is an inelastic scattering interaction which is highly probable when the incident photon energy is much larger than the binding energy of the innermost electron. Since the photon energy is much larger than the binding energy of the atom, it is approximated that the interaction occurs between the photon and a loosely bound or free electron. Due to the massless nature of the photon, to maintain energy and momentum conservation, the photon scatters and energy is transferred to the recoil electron.

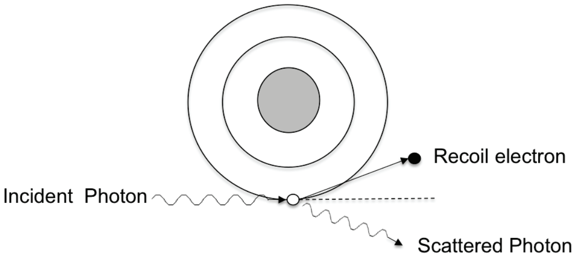

Figure 2.3: Compton scattering

From energy and momentum conservation, the wavelength of the scattered photon λ is related to the wavelength of the incident photon λ_o by eqn. 2.2 where m_o is the rest mass of an electron and θ is the angle between the incident and scattered photon. This equation can also be represented in terms of the energy of the photons by substituting $E = hc/\lambda$ in eqn. 2.2.

$$\lambda_f = \lambda_o + \frac{h}{m_o c}(1 - \cos\theta) \tag{2.2}$$

$$E_f = \frac{E_o}{1 + \frac{E_o}{m_o c^2}(1 - \cos\theta)} \tag{2.3}$$

According to eqn. 2.3, if the angle is 0°, the photon does not scatter because the 'scattered energy' is equal to the initial energy and since there was no energy transfer, no scattering occurred. In Compton scattering, the photon scattering angle can only approach 0° in which the scattered photon energy approaches the initial photon energy which is the maximum scattered photon energy. The scattered photon may range from anywhere above 0° to 180°. However, the angle at which the energy transfer to the recoil electron is a maximum (when the energy transferred to the scattered photon is a minimum) is at 180°. This is observed in eqn. 2.3.

When $1 - \cos\theta$ is at a maximum ($\theta = 180°$), the scattered photon energy is at a minimum as seen in eqn 2.4. Rearranging the equation in terms of the rest mass of the electron in eqn. 2.5 and assuming that the incident photon energy is much larger than the rest mass of an electron, eqn. 2.5 can be approximated as $E_{min} \approx m_o c^2/2 = 255\,keV$, which is the maximum energy of the scattered photon.

$$E_f = \frac{E_o}{1 + \frac{2E_o}{m_o c^2}} \tag{2.4}$$

$$E_f = \frac{m_o c^2}{2(1 + \frac{m_o c^2}{2E_o})} \tag{2.5}$$

The probability of that a photon is scattered through a particular angle is given by the Klein Nishina formula in eqn. 2.6.

$$\frac{d\sigma}{d\Omega} = Zr_0^2 \left(\frac{1}{1+\alpha(1-\cos\theta)}\right)\left(\frac{(1+\cos^2\theta)}{2}\right) \left(1+\frac{\alpha^2(1-\cos\theta)^2}{(1+\cos^2\theta)(1+\alpha(1-\cos\theta))}\right) \tag{2.6}$$

The scattering angle probability is dependent on the atomic number Z, the incident photon energy ν where $\alpha = h\nu/m_oc^2$ (h =Planck's constant, m_o = rest mass of an electron, and c=speed of light), the classical electron radius r_o given a scattering angle, θ (Wernick and Aarsvold, 2004). From the above relationship there is a higher probability of forward scattering of the incident photon at greater energies and the probability of a scattering angle increases linearly as the atomic number increases (Wernick and Aarsvold, 2004).

Pair Production

This interaction involves converting a gamma ray into an electron-positron pair. Since the rest mass of an electron is 511 keV, the minimum energy that the initial gamma ray must possess is 1.022 MeV in order for the interaction to be possible. Shortly after the electron positron pair creation, the positron recombines with an available electron and two 511 keV photons are emitted at the point of collision 180^o apart. This particular interaction is only significant when the gamma ray energy exceeds 1.022 MeV, otherwise pair production does not occur. As previously mentioned, we are usually only concerned with lower energy photons for SPECT imaging.

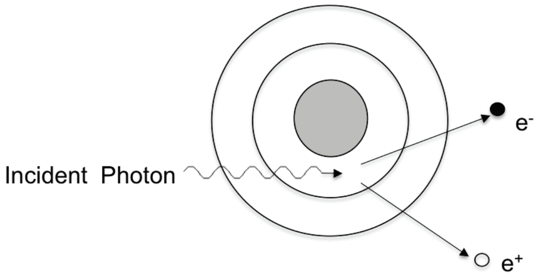

Figure 2.4: Pair Production

2.3 Radiation Detectors

Radiation can be detected directly through gas, liquid filled, and solid state detectors, or indirectly by converting the radiation to lower energy visible light photons via scintillators. A brief summary of each type will be introduced. There will be an emphasis on scintigraphic detectors utilizing solid state technology since we are using silicon photomultipliers for our gamma camera.

Gas Filled Detectors

Gas filled detectors detect radiation by means of creating electron ion pairs in gas, provided there is sufficient energy to overcome the energy required to ionize the gas. A voltage potential is applied to the electrodes on opposite ends of the detector and when an ionization event has occurred, a signal can be measured due to the resultant change in potential (Ahmed, 2007). Depending on the potential applied to the electrodes, gas filled detectors behave differently, and so there exists detectors optimized for each region of operation of voltage potentials. These regions are identified in fig. 2.5 with the pulse amplitude plotted as a function of applied voltage. The relative pulse amplitudes are shown for two different photon energies (Knoll, 2000).

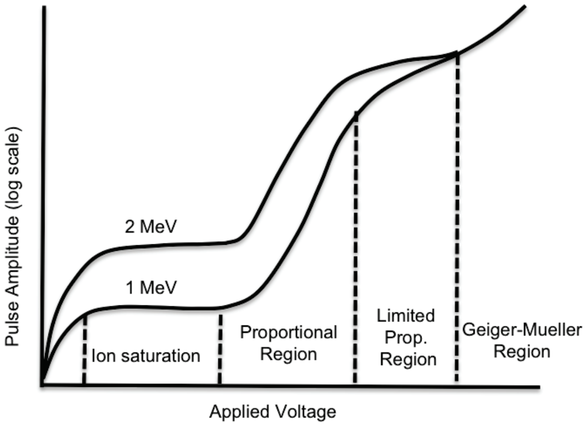

Figure 2.5: Pulse Amplitude versus Applied voltage (Regions of gas-filled detectors)

At very low voltages, there is little to no electric field established, so the charges created by radiation recombine to form neutral atoms. The rate of recombination in this region decreases as voltage increases. So the signals generated by electron-ion pairs which drift to the electrodes do not reflect an accurate representation of the signal because of the amount of recombination (Ahmed, 2007).

The second region is the ion chamber region. In this region, as the voltage is increased, the electron hole pair recombination decreases significantly to the extent where it becomes negligible, though not entirely eliminated. Also, the measured current saturates to some value which is proportional to the energy of the incident gamma ray (Ahmed, 2007).

Beyond the ion chamber region, is the proportional region. With a much larger voltage, a strong electric field exists between the two electrodes accelerating the charge carries to opposite ends. If the electrons have enough energy, they can subsequently create a secondary ionization event. The high electric field can support an avalanche in which the electron from the previous ionization event can go on to create another ionization event. At the electrode, the signal remains proportional to the incident gamma ray (Ahmed, 2007).

The limited proportional region follows the proportional region and is of little importance as the proportionality property breaks down due to an accumulation of positive charges which minimizes the effective electric field (Ahmed, 2007).

Further voltage increases leads to the Geiger Muller region in which multiple avalanches can be created resulting in a very large signal. The signal obtained from a Geiger discharge is the same for all pulses regardless of the number of electron-hole pairs initiating an avalanche (Knoll, 2000). Detectors operating in the Geiger-Muller region are then only used as a counter since there is no distinction between gamma rays of different energies. Gas filled detectors are generally used for detecting fast electron and alpha particles. Typically photon energies of 25-35 eV are required to produce an ion pair (Ahmed, 2007).

Liquid Filled Detectors

Radiation detection can also occur via certain liquids. Incident radiation can generate electron hole pairs in liquids, similar to gases. Since liquids are of higher density than gases, charge pairs have a tendency to undergo recombination. As well, the energy gap between the conduction and valence band of liquids is much smaller, aiding in increasing recombination probability (Ahmed, 2007). However, there are some liquids which exhibit properties in which a significant number of charge pairs are generated with radiation deposition making it a medium by which radiation detection can occur. Common liquids used for radiation detection are liquified noble gases such as liquid Argon, liquid Krypton and liquid Xenon. These liquids usually require about 16-50 eV to produce an ion pair (Ahmed, 2007).

Solid State Detectors

Solid state detectors share many similarities to that of gas filled and liquid filled detectors. The semiconductor detectors discussed in this section relate to direct radiation detection and an emphasis on indirect detection through photodetection will be discussed in a later chapter. The typical energy required to generate an ion pair with solid state detectors is around 3-18 eV per ionization event (Ahmed, 2007). Some of the detectors that will be discussed are silicon diode, germanium, cadmium telluride and cadmium zinc telluride.

Semiconductors

Semiconductors are materials that behave not quite like a conductor nor an insulator. In a conductor, a small band gap exists between the valence band and the conduction band of an atom. When an electric field is applied, electrons move from the valence to the conduction band making them free to move around in the atomic lattice. On the other hand, insulators have a very large band gap. When an electric field is applied, there is insufficient energy for electrons to jump to the next energy level in the conduction band. Semiconductors have band gaps between that of conductors and insulators. At lower temperatures, electrons do not freely move across the band gap, however at higher temperatures, they can be thermally excited to the conduction band. Another way of exciting electrons to the conduction band is via absorption of photons. When an electron is excited, it jumps to the conduction band and leaves behind a hole which behaves like a charge carrier. An adjacent electron will fill that hole generating a hole in place of the electron in the direction of the electric field. The hole essentially behaves like a positron and migrates in the opposite direction of the electron in the conduction band (Serway and Jewett, 2004).

Semiconductors which contain only one element or impurities which do not affect the performance of the material are known as Intrinsic semiconductors. The concentration of electrons and holes are the same. For the purposes of semiconductor photodetectors, doped semiconductors are an essential component to the detection process. By adding impurities, the doped semiconductors are known as extrinsic semiconductors. Depending on the impurities, doped semiconductors can either be n-type or p-type. In n-type materials, there is a higher proportion of negative charge carriers. The energy band from the electron of the donor atom is much closer to the conduction band, thus requiring less energy to excite it to the next level. Whereas p-type semiconductors have impurities which is deficient in an electron, represented by a hole. These excess holes create an energy level near the valence band (Ahmed, 2007).

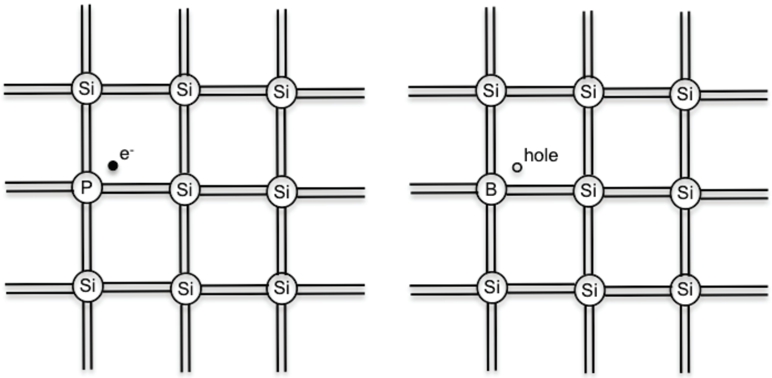

Figure 2.6: N-type (left) and P-type (Right) Semiconductors

The detection of radiation in the semiconductor detector occurs when radiation with energy equal to or exceeding the ionization energy of the material. The ionization energy is greater than the band gap energy because some energy is lost to lattice vibrations. The generation of electron hole pairs is similar to that in gas detectors, except the energy required to create an electron hole pair is much smaller in the semiconductor material. This results in better resolution and sensitivity than the gas detectors (Ahmed, 2007).

P-n junctions

P-n junctions are the basis of photodiodes. They consist of n-type and p-type semiconductors which are joined together. The actual semiconductor itself is a crystal with different dopants to create the n-type side and p-type side. In the absence of an electric field, electrons from the n region will begin to migrate towards the p region and combine with the holes to create negative ions. Likewise, holes will migrate towards the n region and combine with the electrons to create positive ions to balance out charge concentrations. Once the migration of charges have ceased, there remains a space charge region called the depletion region. At the interface of the p-n junction, an electric field is induced by the depletion region which resists further movement of holes and electrons and thus results in zero current.

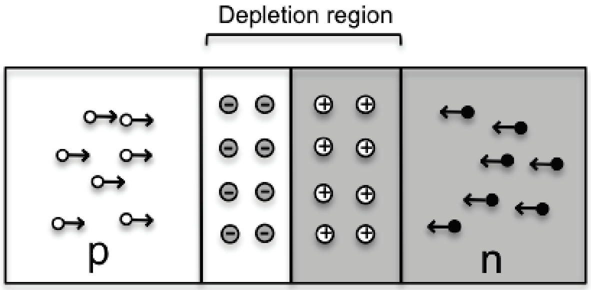

Figure 2.7: P-n junction

There are two ways in which the p-n junction diode can be biased, forward or reversed. For the purposes of detecting photons, forward biased diodes would be inappropriate because an increase in potential would allow electrons to flow in the forward direction towards the p region generating current. Forward biased diodes cause charge carriers to move towards the junction, thus resulting in recombination and current. In the presence of photons or radiation, a continuous current would hinder the ability to determine when a photon is detected. As the forward bias is increased, current will increase linearly and beyond a certain voltage, exponentially. In radiation detector applications, diodes are reversed biased p-n junctions.

Silicon Diode Detector

Silicon semiconductor detectors have a relatively small ionization energy ($\sim 3.6\,eV$) in comparison to gas detectors which require approximately 30 eV to create an ionization event. Contrary to scintillation detectors which require upwards of 100 eV of energy to generate an electron hole pair, a silicon semiconductor detector requires approximately 3.6 eV of energy to create an ionization event. Silicon diode detectors are particularly suited for detecting heavy charged particles such as protons, deuterons, beta particles and fast electrons. However, they are not suitable for gamma ray detection due to their small depletion region width. A more in-depth discussion of semiconductor detectors will follow below in the semiconductor photodetectors section as the basis of operation remains the same. The high energy gamma rays must interact with a scintillator to produce visible light photons to be detected by silicon diode detectors (Knoll, 2000).

Germanium Gamma Ray Detector

Germanium detectors are another type of semiconductor detectors that are generally used for gamma spectroscopy applications. As mentioned previously, a large depletion region is required to detect gamma rays. The width of the depletion region, d is given by the equation 2.7, where V is the bias voltage, e is the electronic charge, ϵ is the dielectric constant and N is the net impurity concentration in the semiconductor material (Knoll, 2000).

$$d = \left(\frac{2\epsilon V}{eN}\right)^{0.5} \tag{2.7}$$

From this equation, the impurity concentration controls the depletion width at some voltage. Germanium detectors can be manufactured to be very pure with minimal impurities called high purity germanium (HPGe) detectors. They have depletion widths up to a few centimetres which allows for detection of gamma rays. The germanium crystal is encapsulated in a vacuum sealed cryostat to maintain it at a very low temperature (77 K). Operating the detector at room temperature would result in significant leakage current due to the small band gap of germanium (Knoll, 2000). As a result, while germanium detectors offer superior energy resolution, their bulky size due to the cooling apparatus and the necessity to maintain low temperatures for accurate performance make them unfavourable for imaging.

Lithium Drifted Silicon Detectors

The silicon diode detectors are unable to achieve depletion depths greater than 1-2 mm due to significant concentrations of impurities. It is much more difficult to eliminate impurities in silicon diode detectors due to the properties of silicon. However, they can be manufactured to have larger depletion widths by lithium ion drifting resulting in a lithium drifted silicon detector (Si(Li)).

By introducing lithium into the silicon, it balances the acceptor and donor impurities resulting in a larger detection volume. The thickness of the active region of the detector is dependent on the amount of lithium drifted into the detector (Knoll, 2000). This lithium drifting process used to be performed with germanium as well, but due to the high mobility of lithium in germanium, there is a tendency to have an unbalanced distribution of lithium. With the development of HPGe detectors, they are preferred over Ge(Li) because it is much more stable to manufacture. Since silicon has a low atomic number (Z=14) compared to germanium (Z=32), the probability of photoelectric interaction is very low. However, for low energy gamma rays, the probability increases making Si(Li) detectors ideal for low energy gamma ray and x-ray spectroscopy (Knoll, 2000).

CdTe and CdZnTe Detectors

Cadmium Telluride (CdTe) and Cadmium Zinc Telluride (CZT) are other types of semiconductor detectors. In an ideal radiation detector, all of the energy from radiation would be absorbed via the photoelectric interaction. However, both silicon and germanium have relatively low atomic numbers, 14 and 32 respectively, resulting in low photoelectric interaction probability. CZT detectors are becoming very popular for imaging applications because of a much larger effective number, 48, resulting in higher energy resolution. In addition, the detection of the high energy gamma rays occur in the CZT detector itself and does not require conversion to lower energy visible light photons. However, one of the biggest drawbacks to developing CZT detectors is their high cost. CdTe detectors are not as popular as CZT because CZT has a slightly larger band gap energy resulting in lower intrinsic free carrier concentration and lower operating surface leakage (Knoll, 2000).

Scintillation Detectors

All of the detectors mentioned thus far have been direct detection. The following section is a discussion on an indirect detection method by means of a scintillator, converting the radiation into visible light photons and subsequently detected by photodetectors. This type of detector has been the back bone of nuclear medicine imaging since the beginning and there will be an emphasis on scintigraphic gamma cameras in this thesis. Scintillation detectors have poorer energy resolution compared to other semiconductor radiation detectors due to the inefficiency of scintillation. Photodetectors only detect approximately 10-15 % of all photons that are incident on the detector. However, they are still widely used due to their ability to perform in relatively stable conditions.

2.4 Gamma Cameras

Gamma cameras are scintillation detectors used in nuclear medicine. They consist of a collimator, detector crystal, light guide, photodetector and signal processing components. The collimator is used to determine where a photon originated from, as scattered photons are eliminated and those that are directly incident on the photodetector will be detected. The next component is the detector crystal or scintillator. Scintillators are materials which emit light when exposed to ionizing radiation. They produce light via the photoelectric effect and Compton scattering. Light guides are used to help spread light out to a larger number of photodetectors so not all of the light is incident on one photodetector for more accurate positioning. Photodetectors then detect these visible light photons. The signals obtained from the photodetectors undergo some signal processing, digitization and positioning to reconstruct an image.

Scintillators

When a high energy gamma ray interacts with a scintillator, it undergoes either the photoelectric effect or Compton scattering followed by the photoelectric effect. Also, the gamma ray could potentially undergo multiple Compton scattering events and scatter out of the scintillator or deposit the remainder of the photon energy via the photoelectric effect. If the energy deposited exceeds the band gap width and is incident on the crystal, an electron is excited to the conduction band. The electron then becomes a mobile charge carrier. Additionally, a hole is left in the valence band which is also a mobile charge carrier. To stabilize the crystal structure, the electron eventually falls down into a lower energy location called a luminescence centre. The electron then jumps down to the lower luminescence centre, emitting a visible light photon. The electron then goes on to recombine with the hole. The scintillation process is illustrated in fig. 2.8 (Ahmed, 2007). The luminescence centers are a result of impurities called activators which serve to convert the gamma ray into a visible photon (Ahmed, 2007). If the gamma ray undergoes Compton scattering, the scattered photon may go on to further Compton scattering or deposit the remaining photon energy via the photoelectric effect and it is possible the photon may not even interact in the crystal. The amount of light produced in a scintillation material is proportional to the energy of the absorbed event (Table 2.1). If all energy of the original photon is lost via photoelectric interaction, a single intensity peak is observed. However, since there is a probability of Compton scattering, there is usually a range of energies below the photopeak that are detected.

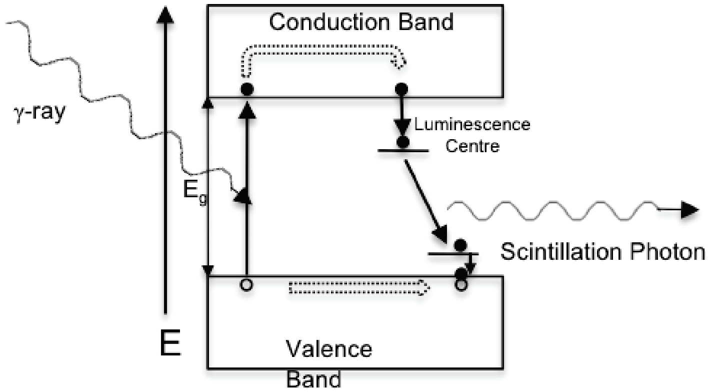

Figure 2.8: Scintillation Process

There is a significant list of factors which affect the quality and performance of scintillators. An ideal scintillator would possess a fast decay time, high conversion efficiency and a high interaction probability. While there doesn't exist a perfect scintillator, there are scintillators which are best suited for one application over another. Some of these factors include stopping power, emission wavelength, light yield, scintillation time and crystal geometry (Wernick and Aarsvold, 2004). Some of these characteristics are listed in table 2.1 (Schotanus et al., 1990; Wernick and Aarsvold, 2004). The intensity of the gamma rays decreases as it traverses the scintillator. The intensity a distance x into the material is related to the mass attenuation coefficient ($\frac{\mu}{\rho}$), and the density of the material (ρ) by the relationship is given by eqn. 2.8. The energy loss in the secondary electrons as it travels through the material is governed by the stopping power. The greater the electron density, the higher the stopping power. For high Z materials and low gamma ray energies, the photoelectric effect is highly probably to occur because the probability of photoelectric interaction, σ_{pe} is proportional to Z^4 (Wernick and Aarsvold, 2004). Conversely, for high Z materials and high gamma ray energies, the probability of Compton scattering is more significant (Wernick and Aarsvold, 2004).

$$I(x) = I_o e^{-(\frac{\mu}{\rho})\rho x} \tag{2.8}$$

Different scintillators are more sensitive in different regions of the electromagnetic spectrum. To optimize the performance of the scintillation detector system, a crystal with an appropriate wavelength emission should be coupled with the subsequent photodetector. Typically, gamma cameras used in SPECT consists of Thallium doped NaI crystals coupled with photomultiplier tubes. NaI(Tl) has maximum emission of photons at 415 nm wavelength which is optimal for PMTs, because they have maximum photon detection efficiency at 400 nm, whereas, CsI(Tl) emits 540 nm photons and SiPMs are most sensitive to photons at 500 nm.

Table 2.1: Common Scintillator Properties

Material	Density (g/cm^3)	Z_{eff}	Max λ (nm)	Decay Time (μs)	Band Gap (eV)	Light Yield (photons/ Mev)
NaI(Tl)	3.67	51	415	0.23	5.9	37 700
CsI(Tl)	4.51	54	540	0.6/3.4	6.4	64 800
CsI(Na)	4.51	54	420	0.63	6.4	38 500
LSO	7.40	65	420	0.04	6	30 000
BGO	7.13	76	505	0.3	5	8200

The length of the scintillation pulses is governed by the decay time of the scintillator. CsI(Tl) has a relatively slow decay time as compared to NaI(Tl). For applications where timing is important, such as PET, CsI(Tl) would not be an ideal crystal. Crystal geometry also plays an important factor in optimizing detector performance. Light emitted from a monolithic crystal is spread out in all directions so that each detector detects a signal. However, it is possible that the light may spread to the point where it may be on the order of background noise. This results in incorrect positioning of the detected event and the energy detected. Adjusting the crystal thickness controls the spread of light, however, if the crystal becomes too thin, ionizing radiation may simply pass right through without interacting with the crystal. Pixelated scintillators consist of smaller crystals lined with reflective material to help guide the photons in a isolated region. A disadvantage of using this crystal is that there may not be sufficient light spread in order to accurately determine the location of the original scintillation event. If all the light is detected by one photodetector, the limiting spatial resolution is the size of the photodetector. To get around this, a glass light guide spreads the light after interaction within the crystal to surrounding photodetectors. The size of the pixellated crystals then becomes the limiting factor affecting the spatial resolution.

Photomultiplier Tubes

The amount of light produced by a scintillator is too small to be visualized without the help of an amplification device. Photomultiplier tubes (PMTs) detect the light emitted from the scintillation crystals and amplify it to a detectable electrical signal. On one end of the PMT is the photocathode where the photons are detected and provided there is sufficient energy to overcome the work function, electrons are ejected. The electrons are accelerated across metal plates called dynodes with large voltage potentials between the plates causing the electrons to undergo impact ionization, generating more electrons at each dynode. At each dynode, one impact ionization will, on average, result in 3 emitted electrons. With 10 dynodes, the typical gain is 3^{10}. The signal is then read out on the anode side of the PMT. This process is shown in fig. 2.9 (Abramowitz and Davidson, 2010).

The subsequent signal processing components help to shape the signal so that the pulse height can be determined. Photomultiplier tubes however can not be operated in a magnetic field, due to the nature of electron acceleration across voltage potentials. The presence of a magnetic field would alter the

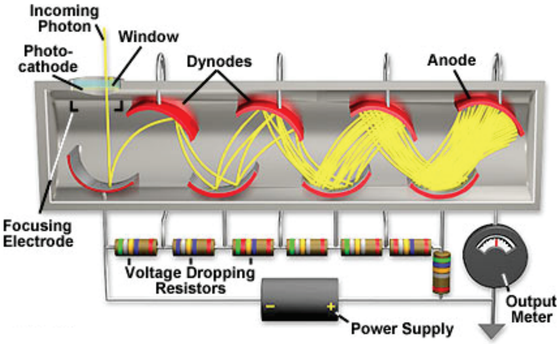

Figure 2.9: Photomultiplier Tube

path of the electrons resulting in incomplete electron collection at the anode.

2.5 Semiconductor Photodetectors

As mentioned previously, high energy gamma rays are not generally measured with semiconductor photodetectors because the depletion width is not large enough. Instead, the high energy gamma rays are first converted to visible light photons via a scintillator. There are several advantages and disadvantages to converting ionization radiation to photons through scintillation. The first advantage being, the semiconductor itself may operate in more stable conditions and is not as susceptible to fluctuations in temperature and other various operating parameters. The main downfall to scintillation detection is its ineffective light production and collection.

Photodiodes are the solid state analog of gas filled detectors as they too have a proportional mode and Geiger mode. The current response of a diode is dependent on the operating voltage. Fig. 2.10 (Collazuol, 2008) represents

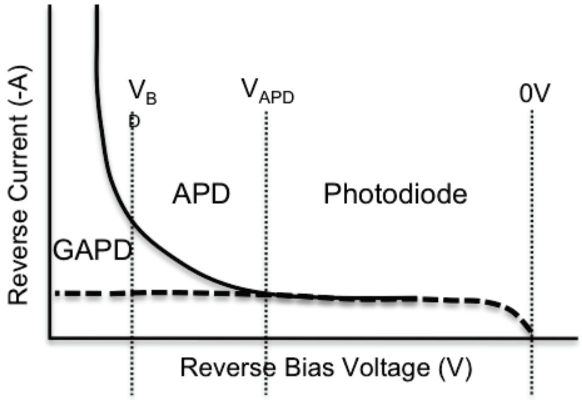

Figure 2.10: I-V Characteristic of Reverse Biased Photodiode

the regions in which a photodiode can be operated and a brief explanation of each type will be discussed with further emphasis on Geiger mode avalanche photodiodes.

Photodiodes

When a photodiode is reverse biased, the internal potential difference push electrons and holes away from the junction and thus very little to no current will flow through the semiconductor. An incident photon of sufficient energy to eject an electron creates an electron-hole pair which drift to the cathode and anode respectively, creating a short burst of current (Ahmed, 2007; Serway and Jewett, 2004). A larger reverse bias increases the electric field across the junction and thus increases the depletion region. Photodiodes are usually used for measuring high photon fluxes since it does not provide any gain (Jackson et al., 2002). In the presence of an external electric field, photons of sufficient energy can generate an electron-hole pair which results in a current. A current pulse is sustained for as long as photons are incident within the depletion region.

Avalanche Photodiodes

Avalanche photodiodes (APDs) are similar to photodiodes except they provide signal amplification through additional impact ionization. APDs are operated at a larger reverse bias voltage than a regular photodiode configuration but below the breakdown voltage, V_{bd}. The breakdown voltage represents the point in which current will begin to rapidly increase (non-proportionatal to the increase in bias voltage). The charge carriers are accelerated due to the electrical potential. The electron gains enough kinetic energy to undergo impact ionization and it may liberate another electron-hole pair as seen in fig. 2.11 (Barral, 2004). The secondary electrons may too undergo impact ionization, thus resulting in an avalanche. The current produced by the charge multiplication is proportional to incident photon energy (Ahmed, 2007; Jackson et al., 2002). However, the gain is limited due to fluctuations in leakage current and shot noise(fluctuations in the current signal) (Collazuol, 2008; Perkin Elmer, 2003; Smith, 2007). APDs are suitable for use in imaging, confocal microscopy and other applications which require high sensitivity and fast response times (Perkin Elmer, 2003).

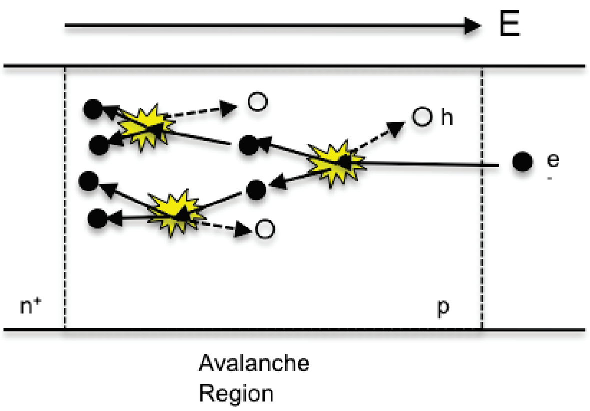

Figure 2.11: Impact Ionization in an Avalanche Photodiode (Barral, 2004)

Silicon Photomultipliers

When an APD is reverse biased beyond the breakdown voltage, the electrons and holes undergo impact ionization at an exponential rate compared to when the APD is operated below breakdown voltage. The breakdown voltage occurs when the current begins to grow exponentially when the bias voltage is increased (Iniewski, 2010). Silicon photomultipliers (SiPM) are a semiconductor radiation detector consisting of thousands of Geiger mode avalanche photodiodes (GAPDs) called microcells.

Each microcell is a p-n junction diode operated with a reverse bias a few volts above the breakdown voltage, V_{bd}. The cross section of the microcell is shown in fig. 2.13. An electric field is established which forces the electrons to drift towards the n doped side of the semiconductor and the holes to drift towards the p side. When a photon is incident in the high electric field region between the p+ and n+ substrate, the energy of the photon generates

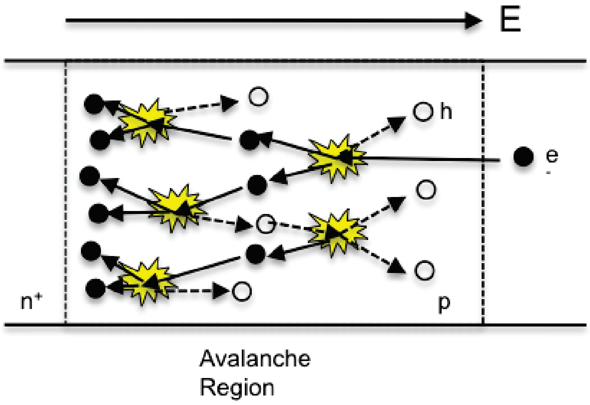

Figure 2.12: Impact Ionization via Geiger Mode (Barral, 2004)

an electron-hole pair. In order for the photon to generate the charge carriers, the energy of the photon must exceed the band gap energy of the silicon material (3.6 eV) (Ahmed, 2007; Iniewski, 2010). Provided the electric field is strong enough, the electron will collide with bound valence electrons and undergo impact ionization, thus generating another electron-hole pair. The additional generated electrons may go on to initiate secondary impact ionizations and those may in turn generate more electron-hole charge carriers thus resulting in an avalanche. The number of electrons generated at the anode is not proportional to the number of incident photons. The output signal of a silicon photomultiplier is the sum of currents from each of the microcells (or micropixels). Because each micropixel is so small, there is a high probability that only one photon will be incident on each microcell. Therefore, the total sum of the micropixels is proportional to the number of incident photons.

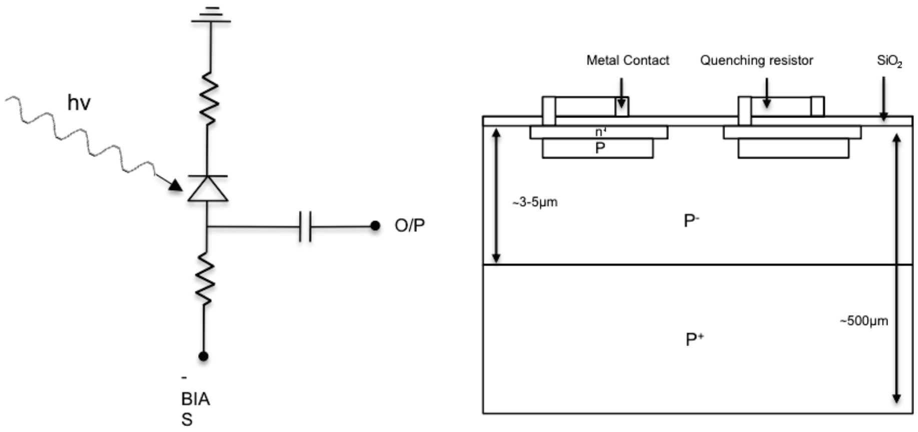

Figure 2.13: SiPM readout circuit (left), Geiger-mode avalanche photodiode structure (right)

Quenching

When an avalanche is triggered, a current signal saturates to some maximum value and plateaus to a steady state current. In order for another event to be detected, the current needs to be quenched and the avalanche process stopped.

There are two forms of quenching, passive, which requires a large resistor and active, which uses an electronic circuit respectively. In a passive quenching circuit, when there is no current through the microcell, the voltage across it is equal to the bias voltage. When an avalanche is triggered, the detector capacitance (C_D) begins to discharge through the series resistor (R_S until the voltage drops below the breakdown voltage with a time constant, $\tau_D = C_D \times R_S$ and the series resistor drops the voltage across the APD. The current grows to an asymptotic limit equal to eqn. 2.9.

$$I_{max} = \frac{V_{bias} - V_{bd}}{R_Q + R_S} \tag{2.9}$$

The voltage drop across the quenching resistor is reduced to below the breakdown voltage. This causes the avalanche to die out because the voltage is no longer large enough to sustain it. Once the avalanche is quenched, the diode is recharged through the quenching resistor. The capacitance is recharged until the voltage returns to the bias voltage with a time constant, $\tau_Q = C_D \times R_Q$. One of the drawbacks of this method is a slow recovery time (Collazuol, 2008; Iniewski, 2010). In the active quenching circuit, instead of a large series resistor, an electronic circuit detects the breakdown and quenches it by discharging the GAPD microcell below the breakdown voltage. The microcell is then recharged with a switch (Aull et al., 2002). The passive quenching circuit is commonly used with SiPMs due to a more compact size and it is less expensive.

Gain

Each microcell generates the same signal from the avalanche. The gain of each microcell can be quantified by eqn. 2.10 with C_{pixel} being the micropixel capacitance, and q_e, the electron charge. The total current signal from each SiPM is proportional to the sum of the number of microcells triggered. Since each microcell produces the same signal, there is less fluctuation in the signal and so SiPM signals are more stable then APDs. As well, the gain has been shown to increase linearly with bias voltage up to 5 V above the breakdown voltage (Collazuol, 2008; McClish et al., 2007).

$$G = (V_{bias} - V_{bd})\frac{C_{pixel}}{q_e} \tag{2.10}$$

Photon Detection Efficiency

In an ideal case, all of the photons produced from the scintillation crystal would be detected by the silicon photomultiplier. However, various factors affect the ability to detect all incident photons. There are three factors which affect the photon detection efficiency (PDE): i) quantum efficiency (QE), ii) the avalanche triggering probability (P_{trig}) and iii) the geometrical efficiency (ϵ_{geom}) as shown in eqn. 2.11 (Collazuol, 2008; Iniewski, 2010). There are two components to quantum efficiency, intrinsic QE, which represents the proportion of photons which generate an electron-hole pair in the high field region of the silicon photomultiplier and the extrinsic QE represents the transmission efficiency of the photons (the number of photons that are incident in the detection region of the SiPM that make it through to the high electric field region). The photons must be detected within the active layer known as the depletion region because of the high probability of recombination of the charge carriers in the undepleted regions. Photons incident within the depletion region of the semiconductor material which generate electron-hole pairs do not necessarily go on to trigger an avalanche. P_{trig} represents the probability that an avalanche is triggered. And finally, the geometrical efficiency represents the active area of the detector to the total area of the detector. Photons can not be detected in the regions where there is dead space. The dead space is the non active region of the detector where photons will not bed detected. This contributes to a much lower detection efficiency due to a relatively large area of dead space on SiPMs. The overall photon detection efficiency increases with bias voltage (Yokoyama et al., 2006).

$$PDE = QE \times P_{trig} \times \epsilon_{geom} \tag{2.11}$$

Another contributing factor to the photon detection efficiency is the structure of the SiPM. The structure affects several characteristics of the performance of the SiPM. The first being the photon detection efficiency and the second being the dark count rate which will be discussed in the following section.

There are two different SiPM arrangements that are optimal depending on the photon wavelength to be detected on the SiPM. The n on p structure is more sensitive to photons in the red region of the spectrum because the longer wavelengths interact deeper in the SiPM. When the electron-hole pairs are generated, the electrons move toward the high electric field region resulting in an avalanche and the holes drift in the opposite direction. If blue light were to interact with the n on p structure, it would most likely be deposited near the surface of the SiPM and the holes would drift through the high electric field region. The probability of impact ionization occurring with holes is less than electrons, therefore light in the red-green region have higher photon detection efficiency with the n on p structure. And conversely, the p on n structure is more suitable for detecting blue light (Iniewski, 2010).

Noise

Factors which affect the noise of silicon photomultipliers include dark counts, afterpulse and optical cross talk. Thermally generated electron hole pairs within the bulk or the surface depleted region at the junction produces a leakage current resulting in dark counts (Collazuol, 2008). The contribution of dark current below the breakdown voltage increases linearly with the bias voltage as a result of surface leakage current. Whereas post breakdown voltage, the current consists of the breakdown current and dark current. Since the microcells operate in Geiger-mode, a dark count may trigger an avalanche thus resulting in an event identical to the single photoelectron. The dark rate of a typical SiPM can be between the kilohertz to megahertz range per square millimetre (Iniewski, 2010).

Afterpulses are a result of impurities within the semiconductor metal which may trap an electron or hole during an avalanche and is released at a later time which may trigger another avalanche (Collazuol, 2008).

Noise from optical cross talk occurs because photons incident on a particular microcell may be absorbed in a different microcell. The probability of cross talk increases with increasing bias voltage (Yokoyama et al., 2006). To minimize the effects from cross talk, SiPMs may have either trenches between each microcell filled with an opaque material or a guard ring may be employed. The overall noise level in SiPMs are approximately around 1 MHz and for SPECT applications this contributes to a lower signal to noise ratio.

Dynamic Range

The dynamic range of the SiPM limits the maximum number of photons which can be detected. Since each microcell detects one photon, if more photons are incident on the detector than there are microcells, then the SiPM saturates. According to Buzhan et al., SiPM saturation occurs when the number of photons (N_{ph}) detected by the SiPM is 60 % of the total number of micropixels, m. This limit accounts for statistical fluctuations in the number of photons and the increase in probability of secondary photons interacting in the detector. The detector response is near linear provided the number of incident photons are small relative to the number of micropixels (Buzhan et al., 2001; Iniewski, 2010).

Conclusions

This introduction of radiation interactions and radiation detectors sets the framework for the purpose of this project. SiPMs are much more compact in size than PMTs, they require much lower operating voltage, only $\sim 30\,V$ versus $\sim 1000\,V$ for PMTs. The most significant advantage to PMTs is their compatibility with magnetic fields. These silicon photomultipliers have the potential to be alternative photodetectors to the rather bulky photomultiplier tubes in gamma cameras.

Three

Applications

3.1 Current Applications

Recently, there has been a significant amount of research with silicon photomultipliers for particle physics and medical imaging applications. Many groups have quantified SiPM performance and there is a multitude of documentation on photon detection efficiency for SiPMs manufactured from various companies. As well, there has been documentation of its dynamic range, gain measurements, dark current and typical energy and spatial resolution measurements for different SiPM models and with various pulse processing electronics (Barral, 2004; Buzhan et al., 2001; McClish et al., 2007; Stapels et al., 2006). A few current applications such as PET imaging, two photon excitation fluoroscopy microscopy, plant imaging, high energy physics, and low photon counting will be discussed.

Low Photon Counting

SiPMs have been shown to have excellent single photon counting capabilities and have been well documented in particular for low light level applications. Published results from (Buzhan et al., 2001; Collazuol, 2008; Iniewski, 2010; McClish et al., 2007; Moser, 2006; SensL, 2010c; Stapels et al., 2006; Yokoyama et al., 2006) and many others indicate that SiPMs are capable of detecting light on the order of photoelectrons. Two potential low photon counting applications where SiPMs could be implemented will be briefly introduced.

Confocal Microscopy

Confocal microscopy was introduced by Marvin Minsky in 1955 as a way to image live specimens by exploiting a fluorescence property in the molecules. A laser is focused to a small volume and as a single molecule passes through the laser, a single photon excites the molecule. The molecule then emits a photon which can be detected by a photodetector. The emitted photons are screened through a pinhole aperture to eliminate those out of focus. The specimen is moved across the imaging plane to image the entire specimen (Semwogerere and Weeks, 2005). This process allows two or three dimensional imaging of live cells.

Two Photon Excitation Microscopy

Two photon excitation microscopy is also a non invasive three dimensional imaging technique which was invented by Denk et al in 1990 (Denk et al., 1990). It involves excitation of fluorophores to image live specimens (So et al., 2000). It is very similar to confocal microscopy except the basis of this imaging technique involves the absorption of two photons causing the molecules to fluoresce. The main difference between a one photon excitation and two photon excitation technique is that the one photon technique, a single photon with enough energy to excite the molecule is absorbed and excites the molecule into a fluorescence stage, whereas in the two photon excitation technique, the absorption of two lower energy photons causes the molecule to fluoresce. With the two photon method, the fluorescence of the cells only occurs at the focal plane of the image resulting in an image that is well focused to the area of interest without the use of a pinhole aperture. A photomultiplier tube is generally used to detect the fluorescence emitted by the fluorophore, but since SiPMs have very good low photon counting abilities, they could be an excellent substitute (Grigorieve et al., 2007).

High Energy Physics

Silicon photomultipliers are being compared to photomultiplier tubes for the purpose of implementing a photodetector system for the front end detector of the electromagnetic barrel calorimeter of the GlueX Project at Jefferson Laboratory, USA. The basis of this project is essentially to discover new excited states of subatomic particles such as mesons by scattering high energy photons (approx 8-10 GeV) from nucleons to create excited states. The SiPMs would be used for detection of the decay products from the mesons to confirm and study the characteristics of the so called 'exotic mesons'. The use of SiPMs indicate better time and energy resolution compared with a photomultiplier tube and so the SiPM is a strong candidate for use in the GlueX project (Kovaltchouk et al., 2005).

Plant Imaging

Another application in which SiPMs have been used is plant imaging. Similar to medical scintigraphic imaging which will be discussed in further detail shortly, plant based imaging uses a positron emitting radiotracer, $^{11}CO_2$ to image plant response to changes in CO_2 levels in the environment. An issue that occurs with imaging plants with positron emitting radiotracers is that due to the thin nature of the plants, the positron may not undergo annhiliation inside the plant. This would affect the ability to accurately image the plant dynamics. A solution to this proposed by Barbosa et al is to use a high strength magnetic field to force the positron to spiral close to the origin of emission and thus allowing the annhiliation to occur near the site of origin (Barbosa et al., 2010). They have developed a detection system using SiPMs manufactured by Hamamatsu coupled with LYSO cyrstals which showed promising results for plant based imaging (Barbosa et al., 2010).

Dual Modality Imaging

Dual modality imaging has become routine in nuclear medicine imaging. Combining scintigraphic imaging with anatomical imaging modalities allows physicians to better diagnose diseases. Computed tomography (CT) offers high resolution anatomical images while SPECT and PET provide images depicting molecular uptake and functional information through radiotracer uptake represented by perfusion, oxygenation and metabolism (Wagenaar et al., 2006). Since scintigraphic imaging is based on functional imaging, it does not necessarily resolve tissue boundaries and image structure within the body. This makes it difficult to localize the area of interest. By complementing it with CT images, one can identify where uptake occurs with respect to anatomical references.

Based on US statistics from 1980, the average effective dose from a CT scan is anywhere between 2-16 mSv and the average effective dose in nuclear medicine is 3-17 mSv depending on what is being imaged (Huda et al., 1989; NCRP, 1989). Due to the relatively high doses delivered to a patient during a SPECT/CT scan, an alternative imaging modality which minimizes exposure to radiation is being explored. Magnetic resonance imaging as briefly discussed earlier does not rely on any ionizing radiation to produce images. As an alternative to CT, MR could potentially become a standard in dual modality imaging. Not only can MR produce high resolution images, one can also perform dynamic imaging depicting various functional processes such as perfusion or metabolism (Wagenaar et al., 2006).

One particular advantage of MR over CT is that MR has excellent soft tissue contrast which would be beneficial for imaging of tumours and other soft tissues. However, there are some major obstacles which need to be considered. The photomultiplier tube in gamma cameras are not compatible with magnetic fields. This is because the signal is dependent on electrons which are accelerated across voltage potentials. They are so sensitive to magnetic fields, such that the gain of PMTs fluctuate depending on it's orientation to the Earth's magnetic field (Wernick and Aarsvold, 2004). To overcome this problem, there is interest in solid state detectors, in particular silicon photomultipliers. They are much more robust than PMTs. The magnetic field compatibility allows us to use SiPMs for a combined dual modality imaging system which could be cost effective. Also, SiPMs are an order of magnitude smaller than PMTs, therefore, it would require less physical space. SiPM temperature can vary over a few degrees during operation but Buzhan et al. reported the SiPM gain to have low sensitivity to V_{bias} and temperature. For a temperature increase of 1°, the gain increased by 0.5 %. Photomultiplier tubes require a warm up time of approximately 30-60 min in order to operate properly (Hamamatsu, 2007). Their performance is strongly dependent on temperature. Fortin reported a significant change in the number of ADC counts from the time the PMT was turned on (room temperature) to it's operation temperature (+6° above room temperature). Over the course of the 40 min warm up period, the number of ADC counts decreased and reached some constant value. The consistent readings post warm up indicate the gain would be stable for operation (Fortin, 2000). SiPMs also have very fast timing resolutions which is ideal for PET. Some of the timing resolutions documented by other groups are mentioned in the following section.

Positron Emission Tomography

Much focus has been centred on dual modality imaging with PET and MR. SiPMs coupled to LYSO crystals have been shown to have excellent timing and energy resolution for PET (Britvitch et al., 2007; Buzhan et al., 2006; Herbert et al., 2007; McClish et al., 2007; McElroy et al., 2007; Schaart et al., 2009; SensL, 2010d). Espana et al. characterized the detector performance in the presence and absence of a strong magnetic field (7 T). The magnetic field had negligible effect on the performance of the SiPM (Espana et al., 2008). Llosa et al. were able to achieve 20 % energy resolution with Na-22 and an LYSO crystal coupled to the SiPM, and a coincidence timing resolution of 1.4 ns (Llosa et al., 2009). McClish et al. reported an energy resolution of 14.4 % using the same crystal and a timing resolution of 0.84 ns (McClish et al., 2007). As a comparison, to the other results, McElroy et al reported an energy resolution of 15 % with the same parameters and a timing resolution of 1.9 ns. The differences between the different groups were the manufacturer of the SiPMs. There energy resolution was quantified with Na-22 with LYSO coupled to the SiPM. These results from the references listed above show potential for dual modality imaging with MR/PET.

Single Photon Emission Tomography

While the basis of the gamma camera for PET and SPECT are essentially the same, there are some distinct differences which must be considered when designing a gamma camera for specific applications. An important difference is that PET requires timing information in order to correspond photon events originating from the same annihilation. As well, only 511 keV photons are detected. Photons of various energies could be detected with SPECT imaging and timing information is not important. There has not been much development in the way of using SiPMs for SPECT applications, however there is a potential for a large market which would benefit from optimizing a silicon photomultiplier based gamma camera for SPECT applications.

Gruber et al. have developed an imaging system with CsI(Tl) and silicon photodiodes for SPECT. While these aren't SiPMs, they obtained relatively good energy and spatial resolution with a form of semiconductor detector. Their results show potential for silicon photodiodes to replace traditional photomultiplier tubes. However, their investigation was not driven by MR compatibility rather, it's intrinsic resolution and compact size (Gruber et al., 1998). They have also identified a need to cool the electronics to optimize the energy resolution (Gruber et al., 1998). While silicon photodiodes have shown to be an option for SPECT imaging, it poses limitations due to the lack of additional gain from the detector itself.

There are numerous sources that have confirmed the compatibility of silicon photomultipliers in magnetic fields as well as energy and spatial resolution comparable to photomultiplier tubes. Applying these to SPECT could result in more stable operation than silicon photodiodes and decrease the size of gamma cameras. As well as to provide the opportunity to operate them in the vicinity of an MR scanner or integrate an MR scanner with a gamma camera for dual modality imaging.

Hawkes et al. are focused on developing PET/MR with SiPMs. Besides a few different key factors that separate SPECT from PET in terms of gamma ray energies, scintillation crystals, readout electronics and photon detection of single or coincident events, the actual acquisition of photons from SiPMs remains the same. They have performed tests of SiPMs in magnetic resonance pulsed fields and have concluded that there is no effect on the SiPM performance in the magnetic field. However, there are concerns regarding the interaction of the MR system with the pulse processing electronics which could lead to deterioration of the MR signal. In addition, heat from the gradient coils may be a factor in SiPM performance (Hawkes et al., 2007).

SensL are investigating their SiPM, SPMArray for SPECT applications. They have obtained a preliminary energy spectrum of a 122 keV peak using CsI(Tl) (SensL, 2010c), but have not published a significant amount of data quantifying the performance of SiPMs for SPECT applications.

More recently, Efthimiou et al. have studied the use of sensL SiPMs for use in medical imaging. Their results were very promising and a comparison between their results and ours will be done in the results section (Efthimiou et al., 2010).

Another group, Majewski et al. performed experiments on Hamamatsu SiPMs. Their studies included NaI(Tl), CsI(Tl) and LYSO crystals. They have also measured the detector performance in a 3 T magnetic field. Similar to Hawkes et al., they noticed that the temperature increase from the gradient coil operation in MRI is a factor on SiPM gain for an SiPM based gamma camera for dual modality imaging with MRI. They obtained the best spectral response with LYSO and a Na-22 at 17.5 % (Majewski et al., 2008).

Since we are not looking at using these SiPMs for PET applications, we are not going to quantify the coincident timing resolution. However, we will quantify the energy resolution with different sources and crystal geometries. A brief comparison between our results and previously published results will be discussed in the results chapter.

Prospective Clinical Applications

Breton et al have investigated the use of dual SPECT/MR imaging for small animal imaging. They acquire SPECT images using the traditional photomultiplier tube followed by an MRI with a low magnetic field strength of 0.1 T (Breton et al., 2007). While a low magnetic field may be sufficient to image small animals, this poses a problem for imaging humans because higher magnetic fields are required to obtain quality images. Based on previous applications discussed, SiPMs have been shown to be a good candidate for most photodetector applications which traditionally utilize photomultiplier tubes.

Our goal is to develop a gamma camera based imaging system with silicon photomultipliers. Once a base system has been developed, the imaging system will have the potential to be scaled to a much larger area. SiPM performance characteristics and baseline measurements first need to be established. An SiPM based gamma camera could potentially lead to a clinical dual modality SPECT/MR system which would allow for simultaneous or sequential imaging to be performed. It is well known that PMTs can not be operated in magnetic fields and SiPMs are insensitive to magnetic fields. By using SiPMs, it is finally feasible to create an SPECT/MR system. SiPMs are much more compact in size than PMTs which make for a more compact system design. An advantage to having a dual modality imaging system over separate imaging systems is improved image registration. Both imaging modalities are secured in place, so co-registering one image to another would be fairly straight forward. As well, with a common patient support, it will be easier to control the effects of patient movement resulting in images that would be easier to register.

A SPECT/MR system could have many potential applications in nuclear medicine. In particular, imaging diseases involving soft tissues such as cardiac diseases, musculoskeletal disorders, or cancer. Musculoskeletal imaging of the hands could benefit from early diagnosis of rheumatoid arthritis as well as monitoring treatment efficacy. MR would provide high contrast imaging of cartilage and joint morphology, whereas the utilization of two radiotracers, Tc-99m which targets bone and In-111 which targets white blood cells depicts bone metabolism and inflammation respectively. The combination of the two imaging modalities allows ones to see functional changes related to the disease with anatomical references prior to morphological changes. Similarly, breast cancer imaging could also benefit from simultaneous SPECT/MR imaging. Mammography is a conventional breast cancer imaging technique which has a high false positive rate (Elmore et al., 1998). One of the downsides to both mammography and clinical breast exams is that the diagnosis is based on a physical abnormality which may or may not be malignant. To overcome this, MR only identifies potential tumours whereas SPECT can trace the biological uptake in tumours which could provide more insight into the extent of the disease and provide a more accurate diagnosis. MR has high sensitivity for detecting breast lesions, but suffers from poor specificity (Goscin et al., 2001). Meanwhile, SPECT imaging using Tc-99m sestamibi provide much higher specificity than MR (Mulero et al., 2000), so the combination of SPECT and MR would improve overall diagnostic accuracy.

Four

Simulations and Hardware Development

4.1 Gamma Camera Simulations

Our eventual goal is to develop a large area gamma camera with silicon photomultiplier photodetectors as a replacement for PMTs. There are many factors that needed to be considered in the gamma camera detector design. A small field of view gamma camera will serve as a prototype for a large area detector. Ideally, our imaging system would possess high energy and spatial resolution while remaining cost effective. As the size of segmented crystals decreases, intrinsic spatial resolution of the detector increases. However, this is not an optimal solution financially as discrete crystals are very expensive. In addition, monolithic crystals provide better energy resolution than discrete crystals because there is some light loss as a result of reflections in the crystal boundaries. In order to evaluate various geometric configurations, we have turned to computer simulations. The gamma camera was simulated in MATLAB using various crystal geometries to compare the reconstructed images and energy spectrums to determine the optimal parameters.

The simulation consists of several parts: generating a simulated source, modelling the detector response, and image reconstruction. In addition, the quantum efficiency and three sources of noise were modelled into the simulation: intrinsic scintillator noise, dark and SiPM noise.

First, the two dimensional source is created by generating a large number of random events representing the true interaction locations with a user defined energy. The size of the detector and the crystal geometry are specified. Intrinsic scintillator noise arises from electron trapping and thermally generated electron hole pairs. This variation in the number of photons detected is modelled with Poisson noise.

The modelled SiPM photodetector consists of a scintillation crystal coupled to a 4×4 array of SiPM pixels with each pixel equal to $3.16\,mm \times 3.16\,mm$. An example is shown below in fig. 4.1 with $2\,mm \times 2\,mm$ crystals. The simulated events generate a number of photons / MeV of energy detected depending on the type of crystal specified. The number of photons per unit area is inversely proportional to the square of the distance from the gamma ray origin. The light response of the simulated events in the scintillator are modelled as a $1/R^2$ relationship shown in eqn. 4.1, where d is the crystal thickness and the position of the detected event is (X,Y).

$$L(x, y, z) = \frac{1}{(x - X)^2 + (y - Y)^2 + (z - d/2)^2} \tag{4.1}$$

The next component of the simulation is the optical diffusion in the light guide. The diffusion of light is characterized by the point spread function (PSF) as in eqn. 4.2. The position in the PSF is given by x and y and σ is the deviation in the distribution. Ideally, a point source when imaged would result in a point source. However, the distribution of light in the light guide represents an isotropic Gaussian response.

$$PSF(x,y) = Ae^{-\frac{x^2+y^2}{2\sigma^2}} \tag{4.2}$$

Quantifying the light detection at the photodetector level is achieved by convolving the light spread function (response in the scintillator) with the PSF (response in the light guide) as represented in eqn. 4.3 (Jahne, 2005). An example of the light response of a random event on the photodetector array is shown in fig 4.1. The overall photon detection efficiency (PDE) is dependent on the active area to the total area of the detector which is already considered in the simulation. However, the quantum efficiency and avalanche triggering probability are not yet accounted for and also contribute to the overall PDE. These parameters and fluctuations in the SiPM signal and dark counts were also modelled in the simulations. To account for fluctuations in the SiPM signal, ±10 % of the raw signal was added/subtracted from the SiPM signal. Dark noise was modelled by adding a random baseline signal to the raw data. The signals are then broken up into the individual SiPM pixels based on the amount of light on each detector.

$$Blur(x, y) = L(x, y) \otimes PSF(x, y) \tag{4.3}$$

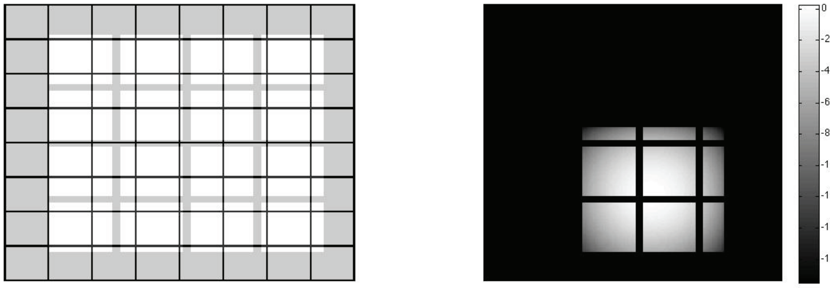

Figure 4.1: 2mm discrete crystal mapped over 4 × 4 SiPM array (left); Light response of a detected event on a 4 × 4 SiPM Array (Right)

The site of photon detection on the detector array is usually accomplished with Anger logic which will be described in the following section. However, there is an inherent spatial distortion effect called edge compression. Generally, this does not significantly affect the outcome of the image so long as the number of photodetector modules isn't too large as image corrections are applied and the distortion is reduced. PMTs are much larger in size than their SiPM counterpart and performing Anger logic on a larger number of photodetectors results in a significant amount of edge compression such that crystals around the perimeter of the detector area can not be easily resolved. Therefore, alternative positioning algorithms are evaluated to determine the optimal method to resolve the majority of the discrete crystals.

Image Reconstruction

We have investigated a variety of positioning algorithms to determine the position of the detected photon as incident on the detector. Reconstructing two-dimensional flood histograms in SPECT imaging is typically accomplished with Anger logic. This method is a common positioning algorithm which only requires four readout channels. In it's simplest form, consider four photodetector modules as seen in fig. 4.2. The x position can be determined by weighting the signal with respect to its position as in eqn. 4.4. The negative x component $(X^- = A + C)$ are subtracted from the positive x component $(X^+ = B + D)$ and divided by the total signal $(X^+ - X^-)$ to determine the x location. Similarly, this same algorithm is performed for the y component by subtracting the negative y component $(Y^- = C + D)$ from the positive y component $(Y^+ = A + B)$ and dividing by the total signal. This algorithm can be expanded to include more photodetectors.

We investigated positioning of events with the 2×2 photodetector Anger logic with our 4×4array system as a means to minimize the number of readout channels. Anger logic is performed simply by dividing our detector area into the four sections and weighting each detector as described in eqn. 4.4. However, as more detection elements are used, it becomes more difficult to resolve the detected events because there is less information to accurately determine the position. This results in severe edge compression. The reconstructed images in fig. 4.3 shows that the detected events corresponding to a crystal element is well resolved in the central region of the field of view but due to edge compression, the crystals cannot be accurately resolved with the 1mm crystals.

The 4x4 photodetector Anger logic method as described in eqn. 4.5 is essentially the same as the 2 × 2 method except there are more readout channels. Weighted sums of the signals depending on the SiPM location is used to determine the position of the incident event. This simplifies to a centre of mass calculation which is investigated in our simulations and described shortly.

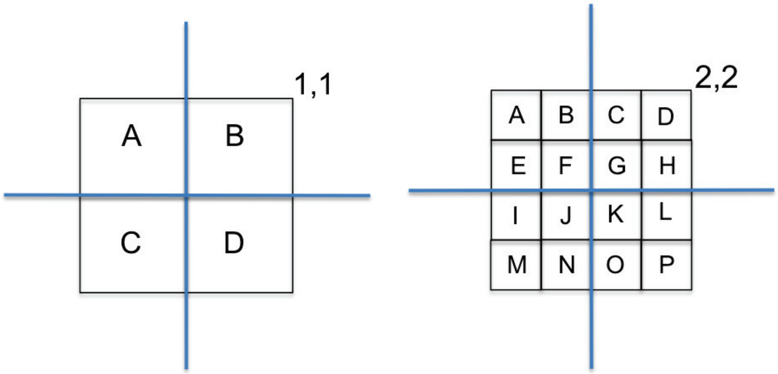

Figure 4.2: 2x2 photodetector for Anger logic (Left), 4x4 photodetector for Anger logic

$$X = \frac{(B + D) - (A - C)}{A + B + C + D} = \frac{X^{+} - X^{-}}{X^{+} + X^{-}} \tag{4.4}$$

$$\begin{aligned} X = {} & [0.75(D + H + L + P) + 0.25(C + G + K + O) \\ & - 0.25(B + F + J + N) - 0.75(A + E + I + M)] / \sum_{i=A}^{P} i \end{aligned} \tag{4.5}$$

In the past, typical gamma cameras containing between 40-100 photomultiplier tubes utilized Anger logic for photon detection positioning. The detection area of a PMT is on the order of at least a couple centimetres ($\sim 2.5 \times 2.5cm$) but the detection elements are of SiPMs are much smaller ($\sim 3.16mm \times 3.16mm$). To create a gamma camera with a practical imaging area, there could potentially be thousands of SiPM pixels. Determining the position of the detected event with a large number of SiPMs would be increasingly difficult to resolve due to the inherent spatial distortions as a result of this positioning algorithm. As an alternative to the traditional 2×2 Anger logic method, other positioning algorithms have been explored to provide a more uniform determination for the spatial distortion correction.

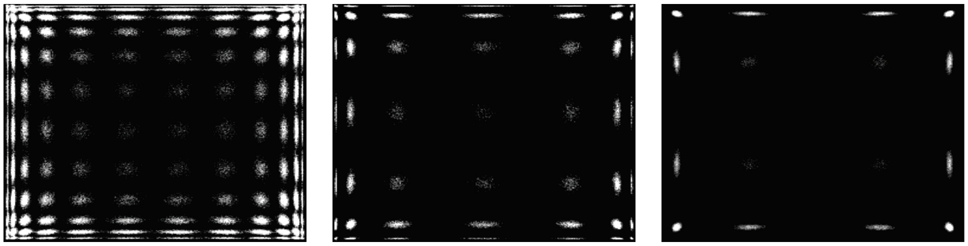

Figure 4.3: Simulated flood histogram of 1,2 and 3mm scintillator reconstructed with Anger logic

One of the methods investigated was a Gaussian fitting. The signals obtained from each of the SiPMs are summed up along the rows and columns of the SiPM array to create signal profiles in the horizontal and vertical dimension. The parameters of a Gaussian function are given by eqn. 4.13 and they are optimized to fit the data from the signal profiles. The width of the pulse is related to the full width at half maximum (FWHM) by eqn. 4.7 and X,Y represents the optimized x and y parameters corresponding to the determined photon location. Fig. 4.4 is simulated flood histograms of 1, 2 and 3mm pixelated scintillators respectively reconstructed with the Gaussian fitting. While the events are more uniformly positioned, the events around the edges are not well resolved because the signal profile towards the edge of the crystal does not represent a Gaussian shape.

$$f(x) = A_x e^{-\frac{(x-X)^2}{2(\sigma_x)^2}} \quad f(y) = A_y e^{-\frac{(y-Y)^2}{2(\sigma_y)^2}} \tag{4.6}$$

$$FWHM = 2\sqrt{2ln2}c \approx 2.35c \tag{4.7}$$

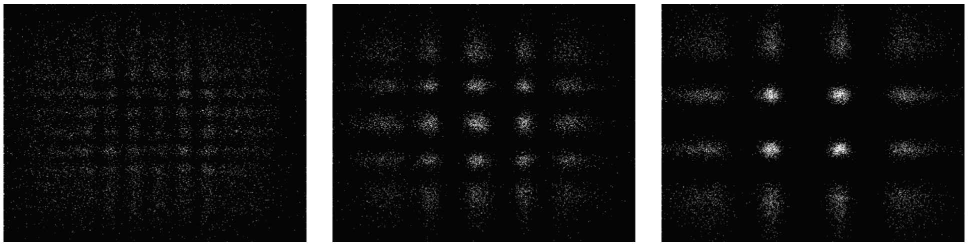

Figure 4.4: Simulated flood histogram of 1,2 and 3mm scintillator reconstructed with a Gaussian fitting

The other positioning algorithm tested is the centroid method, otherwise known as the centre of mass method. This is the same algorithm used to calculate the 4 × 4 photodetector Anger logic method for a 4 × 4 array of SiPMs. The detected event is determined by calculating the weighted sum of the signal to its x and y location as shown in figs. 4.5 and 4.8 which simplify to the same method. This algorithm was able to resolve events around the edges of the crystal very well and with the least spatial distortion which would aid in crystal identification for spatial distortion correction. There was some spatial distortion around the edges but minimal compared to the other algorithms. Positioning a detected event near the edge of the detector using the centroid method inherently biases the position towards the center of the image. This occurs because the positioning is based on a weighted sum of the signals and a detected event on the edge is unevenly weighted. With the 4x4 Anger logic positioning method, the larger number of readout channels used provides less spatial distortion, as there is more information to more accurately determine the position of the event (Fig. 4.5).

$$X = \sum_{i=1}^{n} \frac{x_i s_i}{s_{i:n}} \quad Y = \sum_{i=1}^{n} \frac{y_i s_i}{s_{i:n}} \tag{4.8}$$

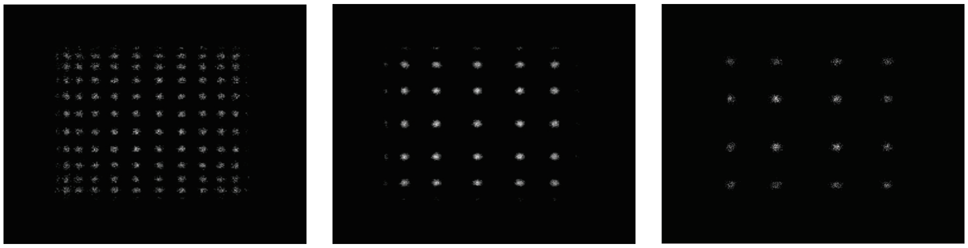

Figure 4.5: Simulated flood histogram of 1, 2 and 3mm scintillator reconstructed with a center of mass fit

In an ideal gamma camera, the detected positions would correspond to the true position across the field of view. The positioning algorithm places the detected events in the best estimated location based on the signals obtained from each readout channel. The reconstructed image will need to be corrected so the detected events correspond to the true position in which the photon was incident.

Scintillation crystal

Pixelated scintillators are much more expensive than their monolithic counterparts but they offer the ability to guide light in a more contained region resulting in high spatial resolution. However, the energy resolution is superior in monolithic scintillators compared to discrete scintillators because there is a higher probability of maximum light collection, whereas photons generated in a discrete scintillator have a higher probability of scattering out of the crystal, being absorbed or undergo multiple reflections at the crystal boundaries resulting in poorer energy resolution. Simulations were performed to determine the expected reconstructed image and energy resolution with various scintillator geometries. A total of four scintillator geometries were simulated as listed in table 4.1 coupled with a 9mm light guide.

Table 4.1: Crystal Geometry

Material	Dimensions	Dead Space	Array
CsI(Tl)	$1mm \times 1mm \times 9mm$	$0.1mm$	12x12
CsI(Tl)	$2mm \times 2mm \times 9mm$	$0.1mm$	6x6
CsI(Tl)	$3mm \times 3mm \times 9mm$	$0.1mm$	4x4
CsI(Tl)	$12mm \times 12mm \times 9mm$	–	1

To determine the spatial resolution with a monolithic crystal, a mask was used such that gamma rays incident on the mask would only penetrate at holes specified at 1 mm, 2 mm and 3 mm increments (Fig 4.6).

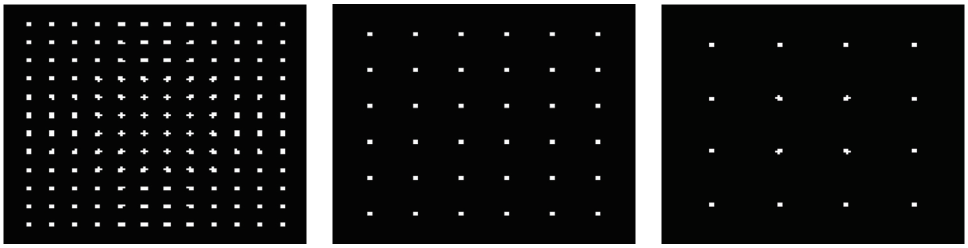

Figure 4.6: 1, 2, 3mm mask for monolithic crystal simulations

The centre of mass algorithm was used to reconstruct the 2D histograms seen in fig. 4.7 and our results show that this algorithm is not ideal for monolithic crystals with a small detection area. The appearance of the reconstructed images with the monolithic crystals is mapped to a smaller area and lacks crystal localization. The other positioning algorithms mentioned earlier were also used with the monolithic crystals, but all methods were unable to localize the detected events accurately. The spatial resolution of the monolithic crystal is poor partially because the detector area is quite small (We are currently simulating one array of an SiPM which is only $13.4\,mm \times 13.4\,mm$). Due to the the small nature of the SiPM Array, there may not be enough of a difference in pixel signals to accurately determine where the light originated from and thus the event is averaged towards the centre of the SiPM array. The signal to noise ratio may be degraded since only a small portion of photons actually make it through the mask. With opportunities for photons to undergo multiple interactions before interacting with the SiPM, photon scattering and noise contribution may hinder accurate event localization.

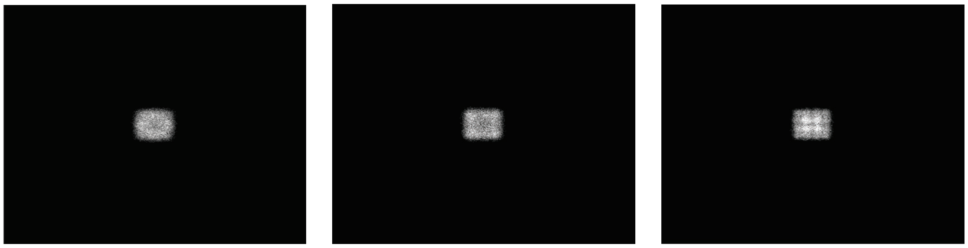

Figure 4.7: Simulated flood histogram of a monolithic scintillator coupled to a mask with holes separated by 1,2 and 3 mm, reconstructed with a center of mass fit (Centroid Method)

From the simulations, it appears monolithic crystals have an inability to image small areas. They could potentially be suitable for larger area detectors. On the other hand, detected events were well resolved with pixelated scintillators as seen in fig. 4.5. For detector characterization of our gamma camera system, pixelated scintillators will be used.

Image Segmentation

The distortion introduced by the grouping of events into clusters from the positioning algorithm affects the spatial resolution and the intrinsic spatial resolution of the gamma camera is limited by the crystal geometry. The detected events need to be repositioned to the corresponding crystal. This is done by creating a segmentation map such that each pixel location corresponds to a discrete crystal. There are various segmentation algorithms which have been used for crystal identification such as Voronoi diagrams (Alva-Sanchez et al., 2010) and the watershed segmentation (Chaudhari et al., 2009).

Crystal identification could be performed manually, however, with the advancement of SPECT imaging, scintillation crystals may consist of thousands of pixelated crystals and it would be too time consuming to manually identify the peaks corresponding to each crystal. A semi-automatic method similar to that proposed by Chaudhari et al. has been implemented (Chaudhari et al., 2009). The segmentation is performed on a template image which is generated by smoothing the reconstructed image with various filters.

The first component of segmenting the image involves filtering to smooth the image. Two types of filtering are used to generate the template image. The segmentation is performed on this template image which is filtered accordingly to allow for accurate segmentation. The first type of filter on our image is a simple Gaussian filter given by eqn. 4.9. The X and Y denotes the two dimensional components of the Gaussian filter, with σ being the standard deviation of the Gaussian distribution (Gonzalez and Woods, 2008). This Gaussian filter takes the discrete image and blurs out the detected events. A second stage of filtering is implemented to eliminate noise. A bilateral filter is a weighted Gaussian filter based on the neighbouring pixels and the intensity values. In this particular filter, the pixel values are averaged over a region in which values are weighted less as one moves further from the central pixel of interest. This method is great for smoothing out regions in an image while preserving edges (Paris, 2007). While there are no sharp lines in the flood histograms, the

Gaussian filter has some noise contribution which makes segmenting the image difficult. The bilateral filter minimizes noise and preserves edges by weighting pixels with similar intensities and pixels in closer proximity heavier. There are two major components to bilateral filtering, the spatial parameter and range of intensities.

$$f(X, Y, \sigma) = e^{-X^2+Y^2/2\sigma^2} \tag{4.9}$$

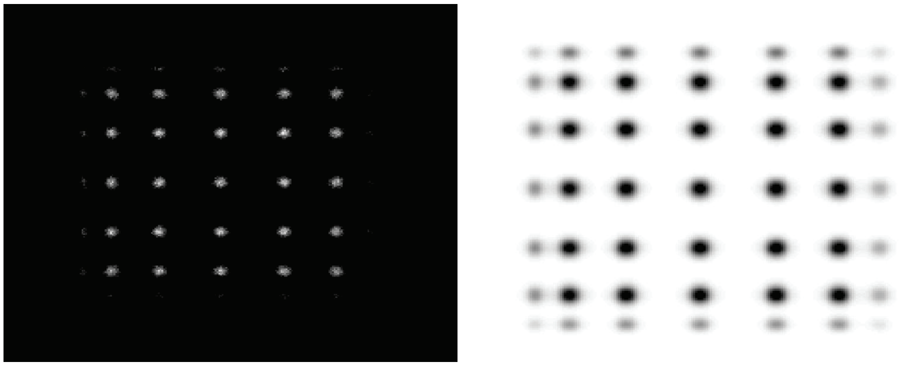

Figure 4.8: Simulated flood histogram of a 2mm pixelated scintillator (left), Inverted bilateral filtered image of simulated flood histogram with 2mm pixelated scintillator (right)

The bilateral filter smooths an image using two parameters, a spatial weighting and pixel intensity range weighting. Kernels are weighted matrices that contain multiplication factors that are applied to each pixel in an image. To filter an image I, two kernels are required, G, the spatial weighting component (Eqn. 4.10) and H, the pixel intensity range (Eqn. 4.11). The kernels G and H change with each pixel location due to a change in weighting of the

Gaussian function which is dependent on how similar pixel values are to the pixel of interest and and the distance from the pixel of interest. By increasing σ_r in eqn. 4.11, this increases the range of pixel values considered. As σ_r approaches ∞ , the image approaches a Gaussian blur. Likewise increasing σ_d in eqn. 4.10 increases the number of pixels in the kernel which affects the smoothness of the image. As σ_d and the kernel area increases, more blur is present in the image (Elad, 2002; Tomasi and Manduchi, 1998). The bilateral filtered image is given by the eqn. 4.12 where I is the image that is being filtered (Zhang, 2009).

$$G = e^{-((i-k)+(j-m))^2/(2\sigma_d^2)} \tag{4.10}$$

$$H = e^{-(I(i,j)-I(k,m))/(2\sigma_r^2)} \tag{4.11}$$

$$B(i,j) = \frac{\sum_{N(k,m)} G_{i,j,k,m} H_{i,j,k,m} I_{i-k,j-m}}{\sum_{k,m} G_{i,j,k,m} H_{i,j,k,m}} \tag{4.12}$$

A watershed based segmentation is performed on the filtered image to determined the crystal boundaries. This is a similar approach to Chaudhari et al.'s crystal identification method. Rather than manually identifying these regions, their semiautomatic method showed similar results to a manual method. The peak position, energy resolution and count uniformity showed insignificant differences between the two methods (Chaudhari et al., 2009). The watershed based segmentation can be explained with a simple example in fig. 4.9. The peaks in the template image can be compared to catchment basins. These catchment basins collect water and the point in which water begins overflowing into another basin denotes a watershed (segmentation line). Attempting to segment the reconstructed image rather than the template image results in oversegmentation as each discrete point acts as a catchment basin. Our segmentation algorithm also allows for the manual peak selection if the watershed segmentation is unable to locate all of the discrete crystals.

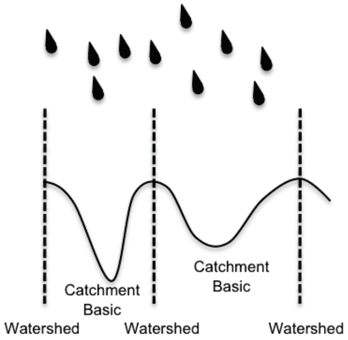

Figure 4.9: Catchment basin analog for watershed-based segmentation (Jørgensen, 2011)

Fig. 4.10 shows the segmentation of the pixelated crystals. Each gray scale shade represents an incremental increase in number of crystals and simply denotes a different crystal. The segmentation map is also overlayed on the reconstructed image identifying the crystal boundaries.

Spatial Distortion Correction

As described in the previous section, the scintillator limits the intrinsic spatial resolution to the size of the detector. A spatial distortion correction was

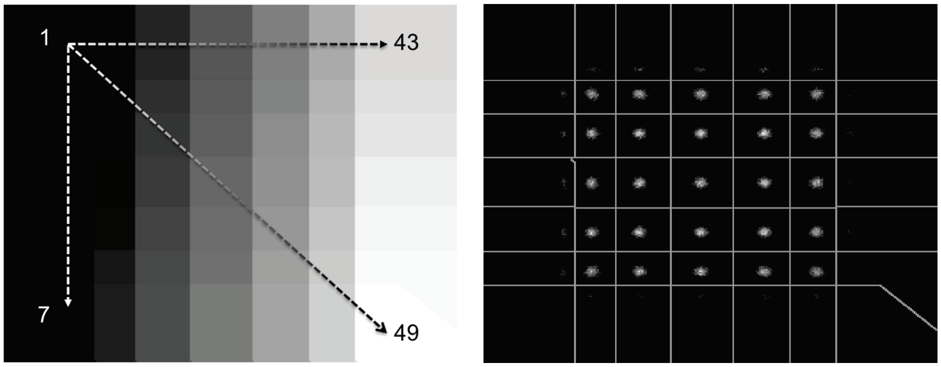

Figure 4.10: Segmentation map of crystals (left) Segmented image (right)

implemented into the simulation to reposition detected events corresponding to the crystal in which it was incident. A look up table is produced such that each pixel location corresponds to a specific discrete crystal as outlined in the segmentation map. The crystal segmentation map varies with different sources because the reconstructed image varies with photon energy (Cherry et al., 2003).

The reconstructed flood histogram is corrected by using the look up table to determine where to reposition the detected events. Fig. 4.11 shows the corrected flood histogram of a 2mm discrete crystal. The corrected image results in a fairly uniform flood image as expected. However, there are some non-uniformities in the corrected image resulting from the crystals partially hanging over the SiPM. The number of detected photons using a flood source should be relatively uniform across the detector area. In fig. 4.11, we can see the SiPMs around the perimeter of the detector area detect a smaller number of photons. This detector nonuniformity is corrected using a uniformity correction map which is discussed next.

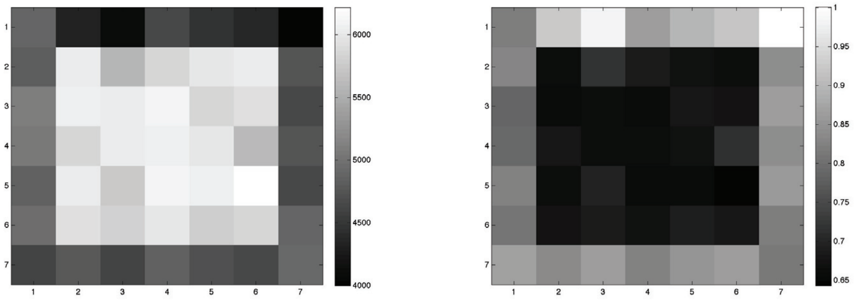

Figure 4.11: Spatial Distortion Correction (left), Uniformity correction map (right)

Spatial Uniformity

Theoretically, a simulated flood source should result in a completely uniform image. However, with the addition of noise, there is some fluctuation in the number of detected photons across the area of the detector. The central region of the detector area is relatively uniform. There is also some significant light loss in the crystals around the perimeter. A spatial uniformity map is used to correct for the nonuniformities in the image. The map is generated by normalizing the inverse of the acquired corrected flood histogram so that the number of detected photons in each crystal is the same. This uniformity correction map is shown in fig. 4.11. Applying this correction map to the corrected spatially distorted image results in an image with a similar number of counts in each crystal.

Energy Correction

The energy resolution is a characteristic which determines how well the detector system can resolve gamma rays of different energies. Theoretically, all detected photons would be measured with the same signal and so the energy spectrum would be a delta function at the photopeak. However, due to differences in light collection, there is a spectrum of detected energies. The corrected spectrum accounts for lower energy photons as a result of dead space within the detector area and is determined by normalizing the photopeak in each discrete crystal element to the the energy corresponding to the photopeak.

To determine the energy resolution, the peak spectrum is fitted to a Gaussian function as described briefly in eqn. 4.13 (Knoll, 2000), where A is the peak area, E_o is the peak energy, and σ, the standard deviation. The quantification of the energy resolution is represented by the full width at half maximum (FWHM) as shown in eqn. 4.7. The energy resolution is simplified to eqn. 4.14 (Knoll, 2000) with a Gaussian curve. The energy resolution of the simulated energy spectrum with a 245 keV source is 31 % and 22 % with the correction.

$$G(E) = \frac{A}{\sigma\sqrt{2\pi}} e^{-\frac{(E-E_o)^2}{2\sigma^2}} \tag{4.13}$$

$$R = \frac{(FWHM)}{E_o} \tag{4.14}$$

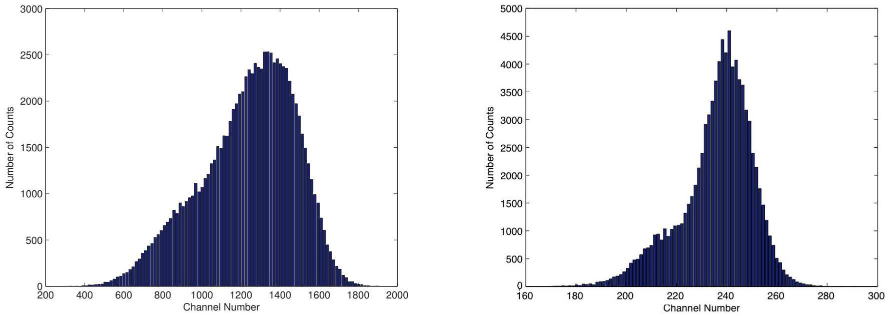

Figure 4.12: Energy Spectrum with 245 keV source (left), Corrected energy spectrum (right)

Gain Correction

Photodetector performance can vary due to slight variations in production. This would result in detected photons occurring in different channels depending on which photodetector it was incident on. Similar to the energy correction, a correction to normalize the peak channel is necessary so that the response is uniform between each photodetector. This is usually necessary with PMTs, however, the fluctuation in the gain of SiPMs does not affect the signal. This is because the signal is dependent on the number of micropixels triggered, not the high gain signal itself. The sum of the micropixels triggered results in a signal proportional to the number of photons. There may be fluctuations in the number of photons generated within each SiPM for a flood source of gamma rays, but it may not be significant. Therefore, a gain correction was not implemented.

4.2 Electronic Instrumentation and Development

Simulations of our proposed gamma camera were performed in conjunction with developing the hardware for our imaging system. Our electronics pulse processing components consist of a charge sensitive preamplifier, pulse height detection circuit and a digital acquisition system (DAQ) for analog to digital conversion. A brief discussion of each of the general pulse processing components are described below, followed by details on our specific hardware development

Preamplifers

Preamplifiers are an essential component to signal processing because the signal measured from radiation detectors are usually very small (on the order of μA and mA) and very fast ($ns - \mu s$ range). Preamplifiers aid in signal processing by amplifying, as well, by lengthening the pulse such that all charges may be collected. It is important to minimize the distance between the preamplifier and the signal source to maximize the signal to noise ratio (SNR) because the cable in which the signal travels along introduces additional capacitance (Knoll, 2000). There are three different variations in which preamplifiers can be operated to optimize the signal output:

- Voltage Sensitive Preamplifier

- Charge Sensitive Preamplifier
- Current Sensitive Preamplifier

The output voltage gain of preamplifiers are dependent on the input voltage in all the configurations listed above. The shape of the output voltage is governed by the instantaneous current in the current sensitive arrangement or by integrating the current pulse in the voltage and charge sensitive arrangement. The appropriate amplifier configuration is chosen depending on the charge collection time which will be discussed below (Ahmed, 2007; Knoll, 2000; Spieler, 2001).

Voltage Sensitive Preamplifiers

Based on the circuit diagram of a voltage sensitive amplifier in fig. 4.13, the input voltage in the amplifier is given by eqn. 4.15. Ideally, the voltage input into the amplifier should be the same as the source voltage. In order to operate the amplifier in this arrangement, the input impedance to the amplifier must be very large (ideally infinite) so the current does not flow into the amplifier. Minimal current should be drawn from the source so that the input voltage into the amplifier is approximately the same as the source voltage. If the input impedance R_i is sufficiently large such that the condition $R_i >> R_s$ is satisfied, then $V_i \approx V_s$, where R_s is the source impedance.

$$v_i = \frac{R_i}{R_s + R_i} v_s \tag{4.15}$$

Fig. 4.14 is a typical circuit arrangement for a voltage sensitive amplifier with C_d representing the capacitance of the detector. When a photon is incident on the semiconductor photodetector, it generates a current pulse in which the total charge is integrated on the detector capacitance from $t = 0$ to $t = t_0$. The source voltage is then approximated by $V_s \approx Q/C_d$ where $Q = \int_0^{t_o} i_s(t)\, dt$. The gain on the input voltage is governed by the electronic components in eqn. 4.16

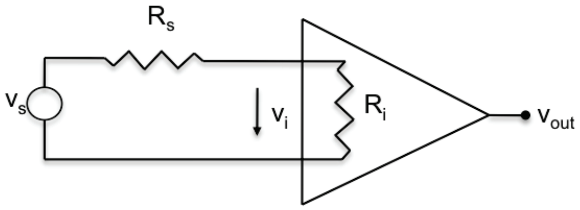

Figure 4.13: Voltage sensitive preamplifier modelled with a voltage source

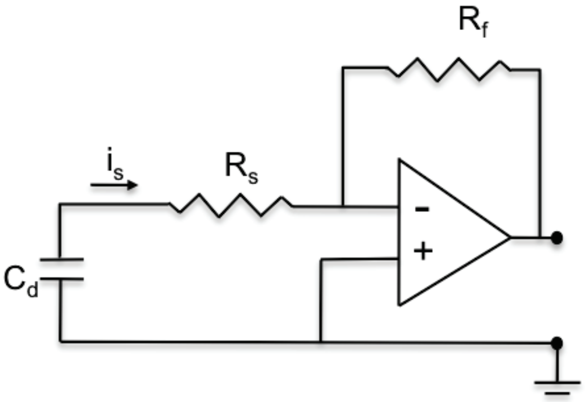

Figure 4.14: Voltage sensitive preamplifier with feedback resistor R_f

$$v_{out} = -\frac{R_f}{R_s} v_{in} \tag{4.16}$$

The time constant R_iC_d should be relatively large compared to the charge collection time t_c in order to ensure full integration of the current signal. One of the disadvantages associated with voltage sensitive amplifiers is that the current pulse is integrated on the detector capacitance. Semiconductor detector capacitance values may change as a result of temperature changes during operation, therefore the output voltage is no longer proportional to the total charge accumulated on the capacitor (Ahmed, 2007; Knoll, 2000; Spieler, 2001).

Current Sensitive Preamplifiers

Current sensitive preamplifiers are different in that the instantaneous current is converted to a voltage signal. This is also known as a current to voltage converter. This configuration is not as commonly used and is optimal when the input impedance is relatively small compared to the source impedance. This results in the current being drawn into the amplifier which results in an output voltage proportional to the input current. Unlike the voltage sensitive configuration, the detector capacitance must discharge faster than the charge collection time in order to ensure the instantaneous current is converted to a voltage signal. Therefore the condition $R_iC_d \ll t_c$ should be satisfied for the current sensitive configuration to be optimal (Spieler, 2001).

The current sensitive amplifier is similar to the voltage sensitive amplifier in that it has the same general structure. The current input is given by eqn. 4.17. If the current amplifier is to convert the current to a voltage,

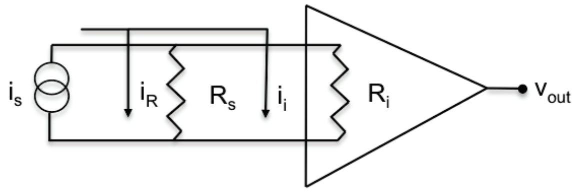

Figure 4.15: Current sensitive preamplifier modelled with a current source

the input current should be equal to the source current. In a perfect arrangement, the input impedance of the operational amplifier will have no resistance. However, in a realistic case, the source impedance should be much larger than the input impedance of the amplifier, $R_i << R_s$ such that $i_s \approx i_i$ since the operational amplifier will always have some impedance associated with it. The current sensitive preamplifier is essentially a current to voltage converter and the output voltage is then proportional to the input current by a factor of the feedback resistor R_f in eqn. 4.18 (Spieler, 2001).

$$i_i = \frac{R_s}{R_i + R_s} i_s \tag{4.17}$$

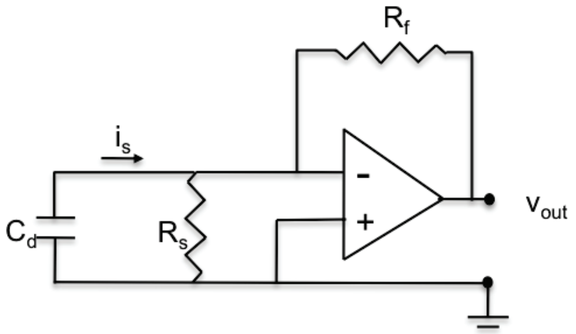

Figure 4.16: Current sensitive preamplifier with feedback resistor R_f

$$v_{out} = -R_f I_{in} \tag{4.18}$$

This arrangement is ideal for when energy information is not as important as obtaining high count rates and accurate timing information (Ahmed, 2007).

Charge Sensitive Preamplifiers

As a solution to suboptimal configuration of voltage sensitive amplifiers to semiconductor detectors, a charge sensitive amplifier is introduced. Instead of integrating the current on the detector capacitance, charge is accumulated on a feedback capacitor. Therefore the output voltage $V_{out} \propto Q_f/C_f$ where Q_f is the charge accumulated on the feedback capacitor C_f and is not dependent on the detector capacitance (Spieler, 2001).

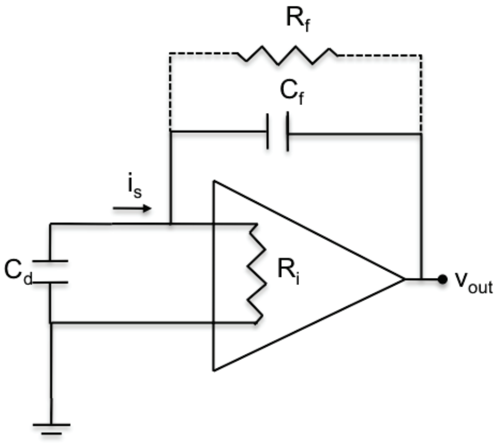

Figure 4.17: Charge sensitive preamplifier with feedback capacitor C_f

The charge sensitive amplifier is widely used in pulse processing with semiconductor detectors due to the negligible detector capacitance parameter. The addition of a feedback resistor is necessary to control the decay time of the pulse. Without it, the voltage signal would be held high due to the accumulation of charge on the feedback capacitor. The decay time is governed by $\tau = R_f C_f$ (Spieler, 2001).

A general guide to determine the appropriate preamplifier configuration is determined by a few criterion. The first is identifying the amplifier impedance. If the amplifier impedance is large compared to the source impedance, the voltage sensitive or charge sensitive configuration is more appropriate. If the time constant is larger than the charge collection time, then the signal is most likely integrated on the detector capacitance or feedback capacitor in the voltage sensitive or charge sensitive configuration respectively.The current sensitive amplifier is more appropriate when the time constant is smaller in comparison to the charge collection time. However, in order for a current sensitive amplifier to operate optimally, the input impedance of the amplifier should be relatively small compared to the source impedance.

Pulse Shaper

Pulse shapers are a common signal processing component. Their main purpose is to eliminate the long tail introduced by the preamplifier and essentially shape the pulse into a Gaussian shape. This prevents pulse pileup from occurring and acts to quickly restore V_{out} to a zero baseline following an event. If the tail of a signal is long and a new event occurs, the voltage signal may ride on top of the previous decaying signal (Knoll, 2000). In our photodetector system, a pulse shaping component was not included because the charge sensitive amplifier has a relatively short decay time ($\sim 25\mu s$).

Pulse Height Detection

The peak detection circuit was programmed so that peak detection only occurs for a short period of time when an event is triggered. The signals are held for a period of time before it is reset. During this time, no other signals are detected and this period of time would represent the detector dead time. The peak detection circuit will be described in further detail shortly. To extract information from the preamplifier signal, the height of the pulse needs to be determined. The pulse passes too quickly for the digital acquisition system to sample the whole pulse due to the relatively fast rise time of the signal from the preamplifier. A specific peak detection circuit is programmed to identify the pulse height and hold it for a specified amount of time to ensure all signals are digitized.

Analog to Digital Conversion

The analog signals need to be converted to a digital signal so that further signal processing such as image reconstruction can be performed. There are various methods of analog to digital converters (ADC) such as a digital ramp

ADC, Wilkinson, successive approximation and flash ADC. These methods are briefly discussed.

Digital Ramp ADC

The digital ramp ADC increases in value with each clock cycle and is compared with the analog input signal via a comparator. When the digital signal is below the analog signal, the comparator output is high. The digital signal will continue to increase until the analog input exceeds the digital signal at which point, the comparator outputs a low signal. The number of clock cycles represents the pulse height. The digital signal is updated into the ADC and resets the ADC. This is not a particularly efficient ADC method because digital conversion of large signals require a longer period of clock cycles to reach the analog pulse height (Kal, 2002).

Wilkinson ADC

Wilkinson ADCs are also known as a linear ramp converters. The input analog signal is compared with a linear ramp signal via a comparator. The comparator outputs a signal which opens a gate until the input signal exceeds the ramp signal at which point the comparator goes low and the gate is closed. A constant frequency square wave is fed through the linear gate. During the time when the gate is opened, the number of pulses produced is proportional to the amplitude of the signal. The number of pulses is tracked by the address register and outputs a digital signal. The time it takes to output the digital signal is proportional to the time it takes for the ramp signal to reach the input pulse height which limits the speed in which the signal is digitized. To minimize the time required for ADC conversion, Wilkinson ADCs are built with clock frequencies of $\sim 100\,MHz$ (Knoll, 2000).

Successive Approximation ADC

Analog to digital conversion of a signal with the successive approximation method is performed by comparing the input pulse to the full scale ADC range. If the signal is in the upper half of the full scale range, a one is entered into the most significant bit (MSB) and half of the full scale ADC range is subtracted from the input pulse. If it is in the opposite region, a 0 is placed in the MSB. In the second stage, the input pulse is then compared with half of the full scale range. Again, if it is in the upper region, a 1 is placed in the next significant bit and half of the current ADC range stage is subtracted from the input pulse, otherwise a 0 is entered. This process is continued until all the bits of the converter is filled. The resolution of the digital signal is limited by the number of bits in the converter. One of the advantages of using a successive approximation ADC is that it takes the same amount of time to convert an analog signal to a digital signal irregardless of the size of the signal (Knoll, 2000).

Flash ADC

An n-bit flash ADC digitizes the input pulse by a series of 2^n comparators with the threshold voltage increasing for each comparator. The input pulse is sent through all the comparators in parallel. For the comparators in which the input pulse is larger than the reference voltage, a logic 1 is outputted. The patterned output from the comparators are converted to a binary number which corresponds to the digital signal (Knoll, 2000).

4.3 SiPM based Radiation Detector Specifications

The schematic of our gamma camera is shown in fig. 4.18. Our system consists of a charge sensitive preamplifier to amplify the signal, followed by a buffer to prevent any signal reflection to the peak detect as a result of impedance mismatching. A monolithic peak detection circuit is used to measure the pulse height of the signal and analog to digital conversion is executed by a digital acquisition system (DAQ).

SiPM/Scintillator - CsI(Tl)

The SiPM selected for this gamma camera is the SPMArrray4 manufactured by SensL which consists of a 4x4 array of SiPMs approximately 3x3mm in size (Fig. 4.19 (SensL, 2010e)). The current model being used for our experiments

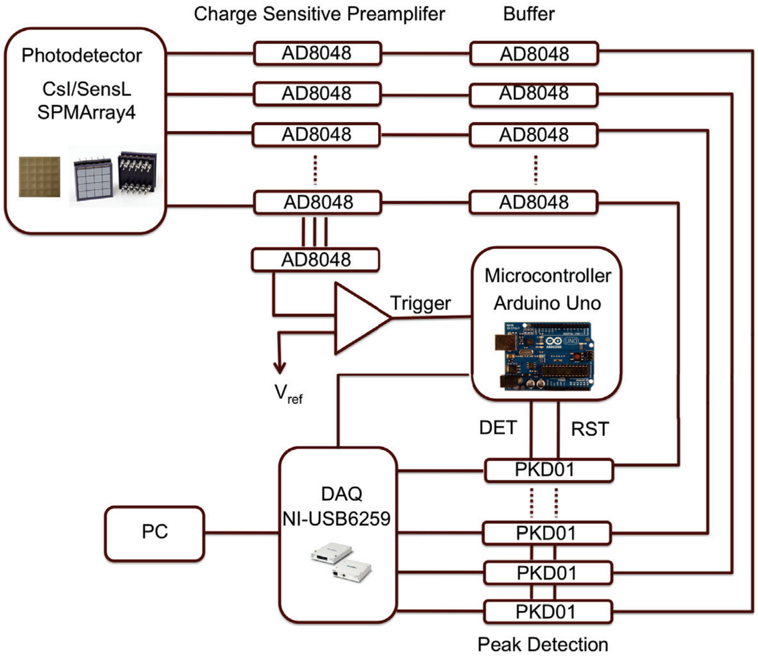

Figure 4.18: Functional Diagram

is the SPMArray4: 305G16. Due to its structure, and small form factor, these SiPMs can be tiled to create a larger area detector. The SiPM specifications and dimensions are listed in table 4.2 and illustrated in fig. 4.20 (SensL, 2009, 2010d). The silicon photomultipliers are insensitive to magnetic fields and so the packaging encasing each of the elements have been developed to be insensitive to magnetic fields as well. Fig 2.13 shows the SiPM readout circuit for one row of the SPMArray4. The SPMArray4 has 16 SiPMs with each row summed on the cathode side of the diode. The signal for each individual SiPM is read out on the anode side of the diode.

The photodetector assembly consists of the SensL SPMArray4 coupled to a pixelated CsI(Tl) crystal with optical grease to minimize light loss

Figure 4.19: SensL SiPM

Table 4.2: SiPM Detector Specifications

SiPM	SensL SPMArray4
Pixel Chip Area	3.16x3.16mm^2
Pixel Active Area	2.85x2.85mm^2
Typical Operating Voltage	29.5V
Pixel to Pixel Spacing	200 μm
Microcell Gain	10^6
Total active area	13.4x13.4 mm^2
Number of microcells	3640/pixel
Dark Rate	8MHz

from photon interaction in air. The emission spectrum of CsI(Tl) peaks at a wavelength of 540 nm (Fig. 4.21 (Saint-Gobain Crystals, 2007; SensL, 2010a)). These SPMArray4s are built with the n on p structure and therefore are most sensitive to light in the red region of the spectrum. The SiPM PDE response as a function of wavelength is shown in fig. 4.21 and shows a peak detection efficiency at 500nm which corresponds with the emission spectrum of CsI(Tl) for optimal light detection (SensL, 2010a). From the simulations of various crystal geometries, the following crystals listed in table 4.3 will be used for characterizing our gamma camera.

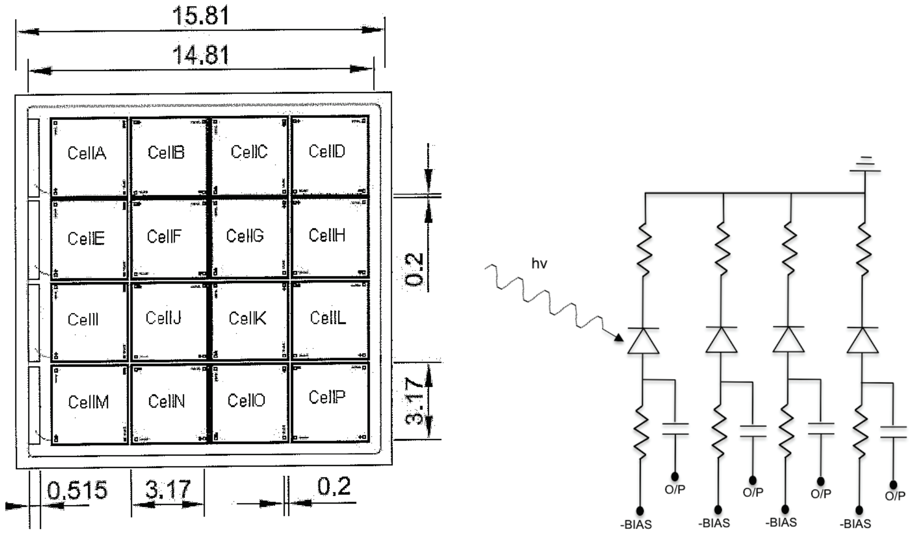

Figure 4.20: Schematic of SensL SiPMArray4 (left), SPMArray4 readout circuit (right)

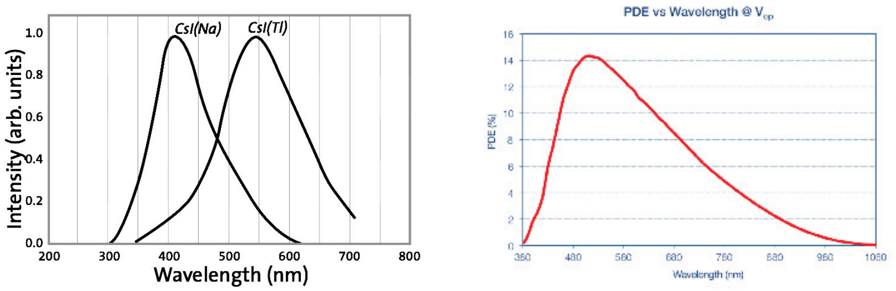

Figure 4.21: Scintillation emission spectrum of CsI (left), SensL SiPMArray4 PDE vs wavelength (right)

Preamplifier - AD8048

The raw signals undergo several pulse processing steps before being digitized. The current signal is initially converted to a voltage signal via a charge sen-

Table 4.3: Crystal Geometry

Material	Dimensions	Dead Space	Array
CsI(Tl)	$2mm \times 2mm \times 6mm$	$< 0.1mm$	6x6
CsI(Tl)	$3mm \times 3mm \times 6mm$	$< 0.1mm$	4x4

sitive preamplifer. Analog Device's AD8048 is a high speed voltage feedback operational amplifier operating in the charge sensitive configuration with feedback components, $C = 100\,pF$ and $R = 47\,k\Omega$. This results in a time constant of $4.7\,\mu s$.

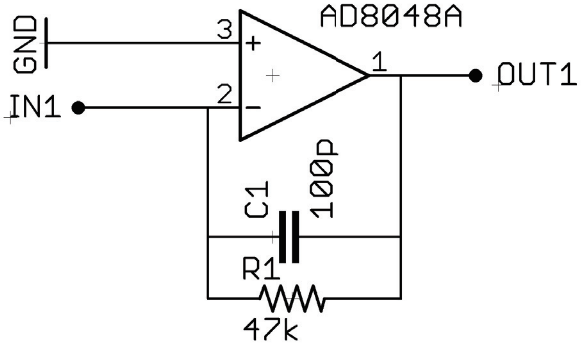

Figure 4.22: Charge Sensitive Preamplifier

The AD8048 operational amplifier has a high gain bandwidth of 250 MHz which allows for high count rates and a high slew rate, (1000 V/μs) to process the full height of the pulse (Analog Devices, 2003).

Using National Instrument's Multisim, a simulated pulse was sent through the AD8048 with various time constants as shown in fig. 4.23. As the time constant increased, the amplitude and pulse length increased as expected with a charge sensitive configuration. The signals are sent through a unity gain buffer

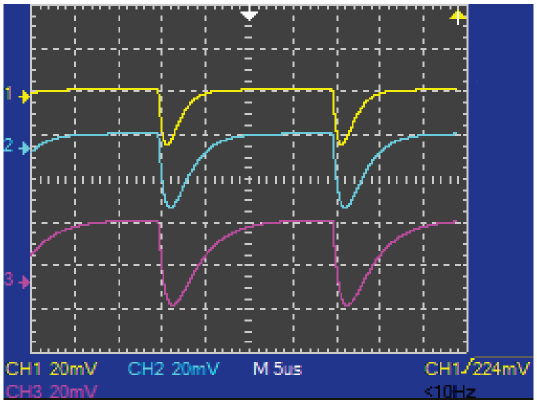

Figure 4.23: Preamplifier Simulation with $R = 10\,k\Omega(1)$, $20\,k\Omega$ (2) and $30\,k\Omega$ (3), $C = 100\,pF$

using the AD8048 operational amplifiers to prevent any signal reflecting from impedance mismatching. The signals are then sent to the peak detect and hold mode chip to determine the pulse height of each channel.

Peak Detection - PKD01

The pulse height detection is performed by a monolithic peak detector with reset and hold mode chip. The peak detect chip detects the peak of the signal and holds the pulse until the signal is digitized. The chip is then reset to digitize the next signal. There are three modes in which the peak detector chip can be operated: detect, hold and reset as outlined in table 4.4 below.

The peak detect chip is initially held in the reset mode.The signals from all 16 channels are summed via a buffer op amp to trigger a detected event. The trigger is fed into the comparator which goes high when the signal exceeds some threshold level indicating a detected event. When an event is triggered,

Table 4.4: PKD Operation Modes

Operational Mode	RST	$\overline{DET}$
Peak Detect	0	0
Peak Hold	0	1
Reset	1	1
Indeterminate	1	0

it enters peak detect mode and the highest signal will be detected, the rest of the signal will be ignored. Once the height of the pulse is reached, the peak detect chip will be sent to hold mode, until all channels have been sampled. The chip is then reset to detect another pulse.

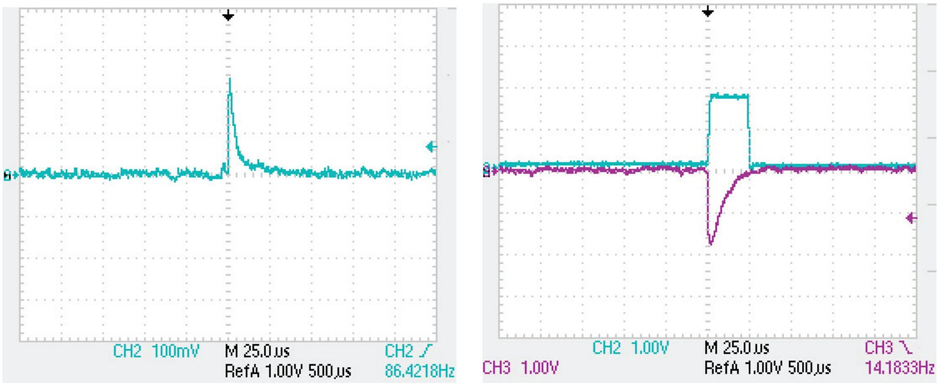

Figure 4.24: SiPM signal before preamplifier (left), SiPM signal after preamplifier (bottom right) & Peak detect output (top right)

The monolithic nature of this chip allows for minimization of charge injection and droop rate errors (Analog Devices, 2001). According to Analog Devices, charge injection occurs from parasitic capacitance resulting in a drop in the signal level. Droop rate errors occur as a result of leakage capacitance which lowers the signal detected on the peak detect chip. The suggested hold capacitor for the PKD01 is $1000\,pF$ and Analog devices reported a slew rate of $0.5\,V/\mu s$. J. Smith performed experiments to determine the optimal hold capacitor (C1) value to maximize slew rate. A $330\,pF$ capacitor resulted in a slew rate of $\sim 1.1 - 1.65\,V/\mu s$ and a $56\,pF$ capacitor resulted in a $6.6\,V/\mu s$ slew rate (Smith, 2007). While decreasing the capacitor helps to improve the slew rate, it also minimizes the amount of charge that can be stored on the capacitor. If the capacitor value was too small, the maximum charge on the capacitor may prevent accurate peak detection. The $330\,pF$ was used in our peak detection circuit to ensure full collection of the SiPM signal while improving the slew rate.

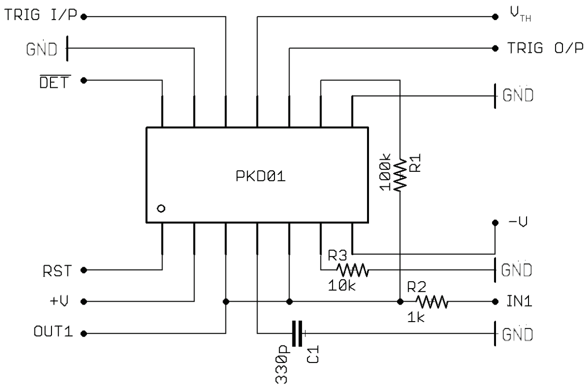

Figure 4.25: PKD01

Analog to Digital Conversion - NI USB-6259/ ATMEL ATmega328 Microcontroller

A National Instruments digital acquisition system (NI-USB 6259 M Series Multifunction DAQ) and an ATMEL 8-bit AVR ATmega328 microcontroller are used to digitize the signal and control the peak detection system. The microcontroller controls the operational mode of the peak detect chip. When an event is triggered from the comparator, it sets the reset (RST) and not-detect ($\overline{DET}$) pin to peak detect for a short period of time ($\sim 8\mu s$), the RST and $\overline{DET}$ are then put into peak hold and is held until all channels have been sampled. The ADC can sample up to a maximum 1.25 MS/s and digitizes the analog signals via a successive approximation architecture. The total time for peak detection and analog to digital conversion is approximately $25\,\mu s$. The microcontroller then resets the PKD01 chip. The microcontroller is also connected to the digital acquisition system (DAQ) to set the clock for signal digitization. The trigger for analog to digital conversion occurs when the PKD01 goes from peak detect to peak hold. Below is the timing diagram of the peak detect RST and $\overline{DET}$ pins, event trigger and interrupt for analog to digital conversion (Fig. 4.26). The event sampling time is determined by the communication between the microcontroller and the trigger signal. The DAQ has 16-bit resolution, maximum voltage range of -10 V to 10 V and maximum clock rate of 1 MHz. The DAQ was programmed to have an input range -5 V to 5 V resulting in a resolution of 0.039 V.

Below is a circuit diagram of our pulse processing electronics for 1 SiPM

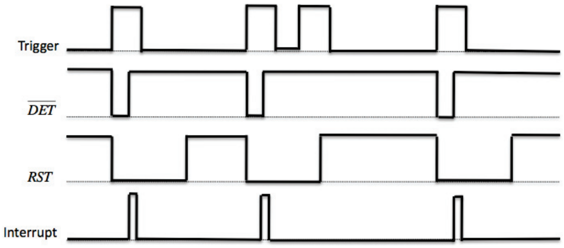

Figure 4.26: Timing diagram of the gamma camera system

channel of our SPMArray 4 matrix. Since the output of the SiPM is biased below -29.5V, an AC coupling capacitor (C=100 pF) is used to block the DC signal and only allow the AC signal to pass through. The result of an AC coupling capacitor shown in fig. 4.27 eliminates the bias voltage portion of the signal. The peak detection circuit is housed on a monolithic chip which provides the peak signal of our input pulse. This is controlled with the RST and $\overline{DET}$ pins and the microcontroller (not shown).

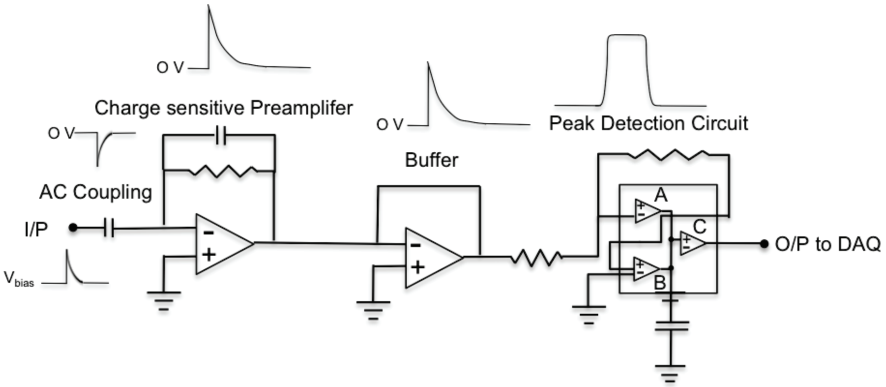

Figure 4.27: Circuit Diagram of one SIPM channel pulse processing electronics

Five

Results and Discussion

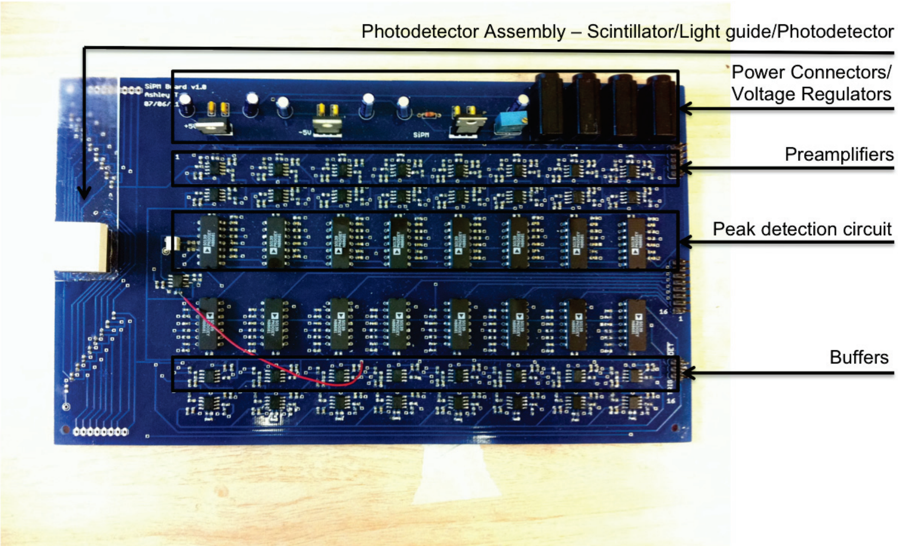

Figure 5.1: Photograph of photodetector (with SiPM) and pulse processing electronics

The SiPM, light guide, crystal and pulse processing electronics were contained on one circuit board and enclosed in a light tight box. The circuit board is shown in fig. 5.1 with the photodetector assembly on the far left. Each channel from the SiPM is fed through the preamplifier, followed by a buffer and the peak detection circuit. The analog signals are then send to the DAQ (DAQ not shown). Our system was set up as shown in the schematic in fig. 5.2. Inside the light tight box, another cover is placed over the photodetector assembly to ensure a light tight system and a lead shield is placed over the source to minimize radiation exposure to the surrounding environment.

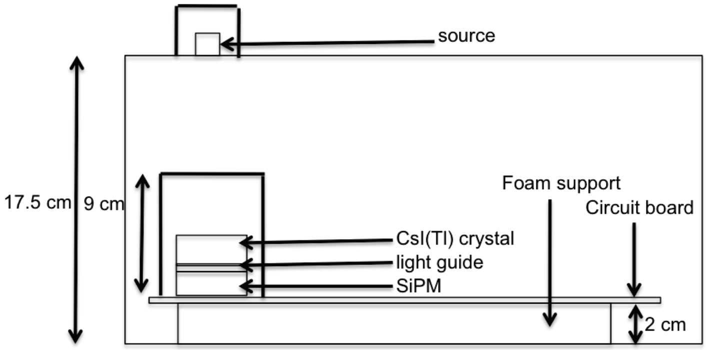

Figure 5.2: Schematic of our experiment set-up

Our experiments consisted of imaging four different sources, Co-57 (122 keV), Tc-99m (140 keV), In-111(171 keV, 245 keV), and Na-22 (511 keV). The measurements outline by NEMA NU1 were used to quantify and maintain clinical gamma camera performance. These include, energy resolution, intrinsic spatial resolution, intrinsic spatial linearity, system uniformity and system sensitivity (NEMA Standards Publication, 2001). The protocols outlined by NEMA are modified to quantify our gamma camera performance. The methods by which each of these measurements were performed are described in each corresponding sections.

5.1 Performance Characteristics

Based on the MATLAB simulations, $2\,mm$ (6×6) and $3\,mm$ (4×4) discrete CsI(Tl) crystals were used in our experiments. The sources were imaged and reconstructed with a centre of mass localization algorithm at five different reverse bias voltage levels ranging from 30.5 V to 34.5 V (1-5 V above breakdown voltage). The images in figs. 5.3 and 5.4 were acquired with a 3mm (4x4) and 2mm (6x6) CsI(Tl) crystal respectively at a bias voltage of 32.5 V. The detected events on the SiPMs are well resolved over a wide range of photon energies and they are comparable to the simulations as seen in fig. 5.5.

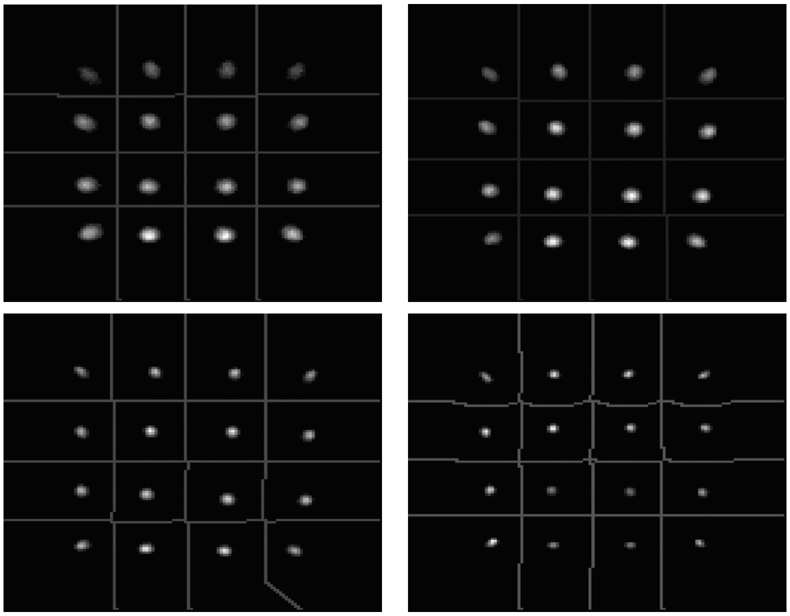

Figure 5.3: Reconstructed images using COM algorithm with superimposed segmentation map. SiPM coupled with 3 mm CsI(Tl) crystal: Co-57 (top left), Tc-99m (top right), In-111 (bottom left), and Na-22 (bottom right)

The figures in 5.4 shows simulated reconstructed image of a 140 keV peak source on the left, and a 511 keV peak source on the right at a bias voltage of 31.5V. The simulations used a $2\,mm \times 2\,mm \times 6\,mm$ discrete crystal for both sources and are a good approximation to the gamma camera performance. The experimental images may also appear to be slightly different depending on the alignment of the crystal to the SiPM as well as the individual performance of each SiPM in the array. Overall, there is a relationship between the peak energy to the resolution of the crystals in the reconstructed image. Images obtained with lower energy sources are less distinct (more blurring) because there are a smaller number of visible light photons produced and the statistical fluctuations in the number of photons contributes more significantly than with a larger number of photons.

The goal is to develop the gamma camera for compatibility with magnetic resonance. Therefore, it is necessary to test the performance of the gamma camera within a magnetic field. The gamma camera system was subjected to a 130 mT magnetic field from a permanent magnet. Fig. 5.6 compares the reconstructed image of a Co-57 source with a $2\,mm \times 2\,mm$ crystal in the absence and presence of a magnetic field. There is no significant spatial distortion in the image with the magnetic field. However, there is some slight blurring compared to the image without the magnetic field. Typical magnetic fields in clinical MRI machines are approximately between 1.5-3 T, which is significantly larger than the magnetic field tested. These results certainly do not eliminate the possibility of spatial distortion at larger magnetic fields. At

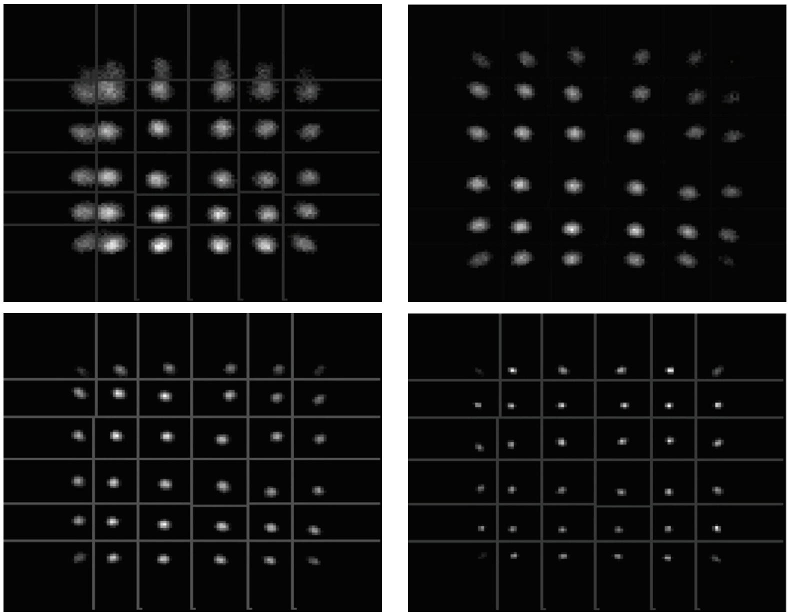

Figure 5.4: Reconstructed images using COM algorithm with superimposed segmentation map. SiPM coupled with 2 mm CsI(Tl) crystal: Co-57 (top left), Tc-99m (top right), In-111 (bottom left), and Na-22 (bottom right

larger magnetic fields, there may be some effects as a result of the changing magnetic fields during MRI operation (ie. when the gradient magnetic fields are turned on and off). However, these initial results are promising for further developments and our gamma camera will be tested within a larger magnetic field environment. We do not expect any influence on the performance of the SiPM with larger magnetic fields, but the magnetic field could potentially affect the electronics of our pulse processing components such as the microcontroller.

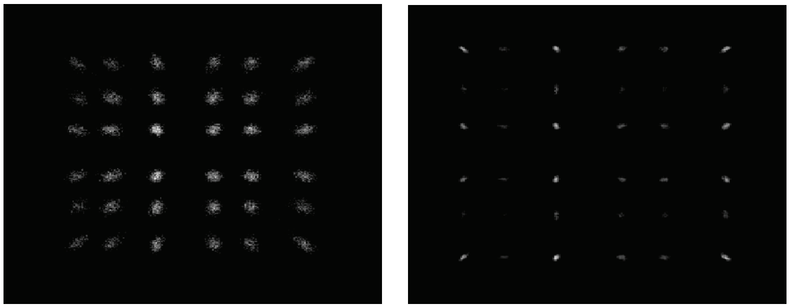

Figure 5.5: Gamma camera simulation (SiPM coupled with 2 mm CsI(Tl) crystal) using COM algorithm: Tc-99m (left) and Na-22 (right)

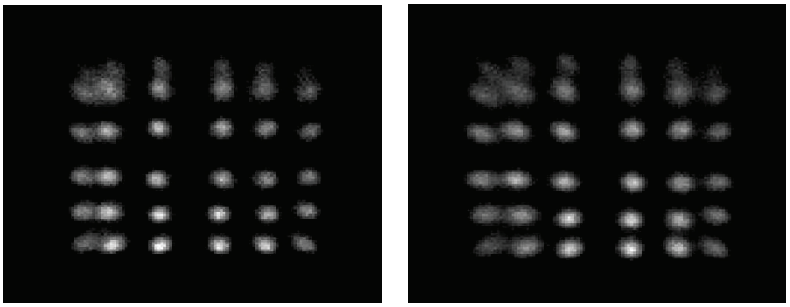

Figure 5.6: Reconstructed image using COM algorithm. SiPM coupled with 2 mm CsI(Tl) crystal: Co-57 (left), Co-57 in the presence of a magnetic field (right)

Energy Resolution

The spectral response of scintillation detectors is relatively poor compared to other forms of detectors such as semiconductors because of the low quantum efficiency, but it remains sufficient for medical imaging applications (Knoll, 2000). As mentioned previously, the smaller the crystal pixels, the poorer the energy resolution. Monolithic crystals enhance energy resolution by ensuring full light collection. Incomplete light collection occurs in pixelated crystals due to the many boundaries in which photons can undergo more interactions, thus resulting in loss of energy via scattering or absorption. The energy resolution is defined by the FWHM divided by the center of the peak.

The detected photon energies are corrected on a crystal by crystal basis. Photons which are detected in discrete crystals should register the same energy peak. However, due to several factors, the amount of light detected may not be the same. There are a few factors which affect the energy of a detected event. There is a statistical variation in the number of photons generated from the scintillator and detected on the SiPM (PDE). Due to the geometric efficiency of these photodetectors, there is a relatively large contribution to dead space. Photons incident within the dead space of the detector will not be accounted for resulting in an energy lower than expected. The total number of photons incident on the detector can vary from each scintillation event which is proportional to the energy of the gamma ray. As well, photons incident on the edges of the crystals may interact and scatter out of the crystal which contributes to loss of light. This variation of peak energy in each crystal warrants a correction such that the intended photopeak occurs in the same detection channel. Each pixel in the image corresponds to a crystal and has an associated energy spectrum.

The segmentation map is used to generate energy spectrums for each discrete crystal element. The calibration curve is made up of the photopeak channels for each source imaged (Co-57, Tc-99m, In-111(2 peaks), and Na-22) and plotted against the true energy respectively (122 keV, 140 keV, 171 keV, 245 keV, and 511 keV) (Cherry et al., 2003; NCHPS, 2011; Perkin Elmer, 1999; Safety and Health, 2010). At low energies, the calibration curve is relatively linear, however a quadratic relationship at higher energies is more appropriate. This curve shows the SiPM linearity. The point at which the curve plateaus, two gamma rays of energies along this portion of the curve can not be distinguished from one another. As stated previously, the number of micropixels limits the number of photons which can be detected and thus limits the maximum gamma ray energy which can be resolved. An example of a calibration curve for one crystal is seen in fig. 5.7. According to the calibration curve, we are approaching the limit of our detection system as the curve begins to plateau out. We are well in the linear range of photon energies for the purpose of SPECT imaging.

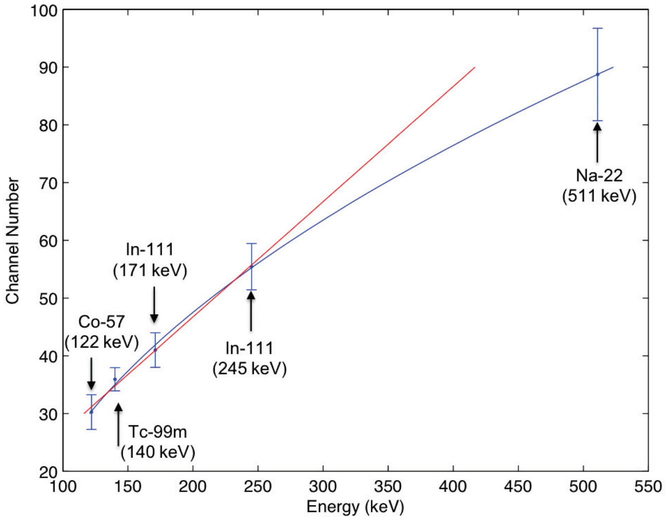

Figure 5.7: Calibration curve - $2\,mm \times 2\,mm$ CsI(Tl) crystal element (@ Bias Voltage = 32.5V)

After the energy correction, the detector response function was measured at each reverse bias voltage level for four different sources. The results of the energy resolution are shown in table 5.1. These results were performed with a 3 mm pixelated CsI(Tl) crystal and calculated with the calibration curve fitted with a quadratic curve. Using the polyfit function in MATLAB, the polynomial coefficients for a quadratic function were optimized to fit the relationship between the gamma ray energy and detected energy. The equation for the optimized quadratic function for the above calibration curve is given by:

$$Energy = -0.0002Channel^2 + 0.27Channel + 0.84 \tag{5.1}$$

There is a general trend that energy resolution improves with photon energy. As the reverse bias voltage increases, the energy resolution deteriorates. We were able to obtain a resolution of $\sim 30\,\%$ with a Tc-99m source and $11\,\%$ with Na-22. The Na-22 source isn't important for SPECT imaging, however, the source was used for characterization of our gamma camera and to quantify the range of photon energies. We performed a comparison of the spectral resolution quantification with both the quadratic and linear fit to see how the values deviate from one another. Na-22 was omitted from the linear fit because at higher energies, the detector response deviates from a linear relationship. Each set of experiments were performed on three separate days to measure the stability and reproducibility of our results.

Table 5.2 summarizes the energy resolution using a linear calibration

Table 5.1: Energy Resolution - 3mm (quadratic fit)

VBias (V)	Co-57 (122 kev) $\Delta E/E$ %	Tc-99m (140 keV) $\Delta E/E$ %	In-111 (171 keV) $\Delta E/E$ %	In-111 (245 keV) $\Delta E/E$ %	Na-22 (511 keV) $\Delta E/E$ %
30.5	33±2	30±1	34±4	21±2	11±1
31.5	33±4	33±2	32±6	23±3	18±2
32.5	36±2	34±3	31±2	24±7	22±5
33.5	36±3	35±4	33±6	20±4	22±5
34.5	35±3	36±4	33±4	21±4	23±5

curve represented by eqn. 5.2. The energy resolution of the two different calibration curves for each source at each bias voltage were similar to one another and for the most part was within the statistical error except for a few sources with a bias voltage of 34.5 V. Values for Na-22 were not included because the relationship is not linear at high energies.

$$Energy = 0.2Channel + 6.78 \tag{5.2}$$

Table 5.2: Energy resolution - 3mm (linear fit)

VBias (V)	Co-57 (122 kev) $\Delta E/E$ %	Tc-99m (140 keV) $\Delta E/E$ %	In-111 (171 keV) $\Delta E/E$ %	In-111 (245 keV) $\Delta E/E$ %	Na-22 (511 keV) $\Delta E/E$ %
30.5	33±1	30±2	34±4	22±4	-
31.5	34±7	31±2	32±6	21±6	-
32.5	33±3	33±2	31±8	23±3	-
33.5	34±5	25±7	32±2	26±5	-
34.5	24±6	24±3	34±5	28±4	-

The results of the 3 mm crystal were pretty stable over the course of several days. However, our results show that the resolution of the 171 keV peak (In-111) is poorer than the 140 keV peak (Tc-99m) at the majority of bias voltage levels in both the quadratic and linear fit.

Comparing these results to previously published results, we were able to obtain superior energy resolution with Na-22. Other groups determined the optimal performance to be with LYSO and Na-22. However, we used CsI(Tl) and reported less than 20 % energy resolution. SensL reported an energy resolution of 14 % for a Na-22 source with their SiPM coupled to LYSO (SensL, 2010b). While the scintillator may be different, we were able to achieve an energy resolution of approximately the same level. It was not our primary objective to have very fast scintillators since SPECT doesn't require any timing information, rather the scintillator should have high conversion efficiency to optimize the energy resolution. CsI(Tl) is a relatively slow scintillator compared to LYSO which is more suitable for timing applications in PET.

Efthimiou et al. also published results in which the energy resolution of the 140 keV peak was superior to the 171 keV peak. We used very similar SensL SiPM models at similar bias voltages. Our quantified energy resolutions at different peak energies are very similar to one another with Efthimiou reporting slightly better energy resolution as seen in table 5.3. This may be a result of the use of a single monolithic crystal. Measurements were also obtained with a 2 mm pixelated crystal at a reverse bias voltage of 30.5 V. These results are shown in italics in table 5.3 and has slightly poorer energy resolution than the 3 mm crystal. A 130 mT magnet was placed adjacent to the photodetector on the gamma camera system to confirm the compatibility in magnetic fields.

The energy resolution as reported in table 5.4 does not deviate significantly from the values obtained without a magnet.

Table 5.3: Energy resolution - CsI(Tl) crystal (2 mm x 2 mm)

VBias (V)	Co-57 (122 keV) $\Delta E/E$ %	Tc-99m (140 keV) $\Delta E/E$ %	In-111 (171 keV) $\Delta E/E$ %	In-111 (245 keV) $\Delta E/E$ %	Na-22 (511 keV) $\Delta E/E$ %
30.5	35±3	28±2	37±3	25±5	17±4
30.5	*N/A*	*25*	*27*	*21*	*14*

Table 5.4: Energy resolution with magnet

CsI(Tl)		2 mmx2 mm	3 mmx3 mm
Source	Energy (keV)	$\Delta E/E$ (%)	$\Delta E/E$ (%)
Co-57	122	33 ± 3	32± 3
Na-22	511	19 ± 3	13 ± 2

Fig. 5.8 shows the corrected energy spectrums of all the different sources. The lower energy sources such as Co-57, Tc-99m and In-111 do not have significant energy spectrum characteristics except for the full energy peak. Na-22 on the other hand exhibits a Compton continuum with a backscatter peak and Compton edge. The energy spectrum of the Co-57 and Na-22 source with the magnetic field is superimposed on the energy spectrums without the magnetic field. There is no significant differences in the spectrums as is with the energy resolution.

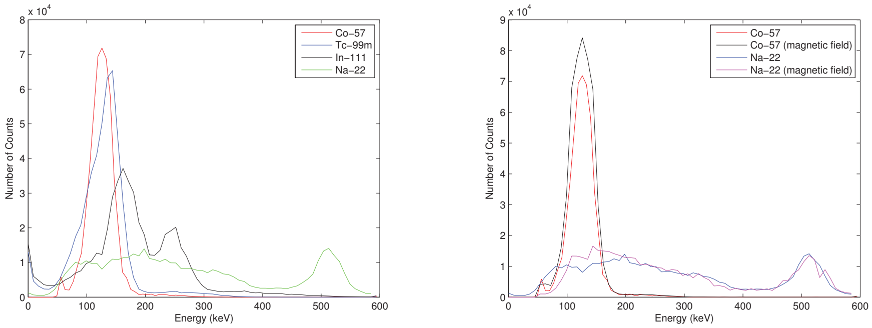

Figure 5.8: Corrected energy spectrum of all sources (left), Energy spectrum of Co-57 an Na-22 - magnetic field (right)

Spatial Resolution

From the reconstructed images, it is clear that the detected events are well separated and $2\,mm$ (6×6) crystals are well resolved. However, the reconstructed image only represents the approximate location as a result of the positioning algorithm. As explained in the simulation section, the intrinsic spatial resolution is limited by the crystal size. Using the look up table from the segmentation maps, the positioned events are repositioned to the corresponding crystal. The image in fig. 5.9 was corrected with a spatial distortion and non-uniformity correction. This corrected image is exactly what we expected, a uniform flood histogram.

From the NEMA NU 1 protocols, there are two measurements to quantify the uniformity, the integral and differential uniformity (NEMA Standards Publication, 2001). The integral uniformity is the maximum deviation in the number of detected counts across the useful field of view (UFOV) and the dif-

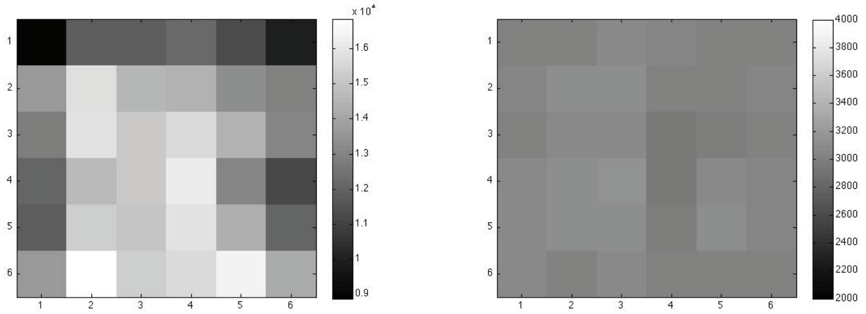

Figure 5.9: Corrected flood histogram of a Tc-99m source with $2\,mm \times 2\,mm$ scintillator

ferential uniformity is the maximum deviation over a limited range around the detector size. In the case of a traditional photomultiplier tube based gamma camera, the differential uniformity would be a practical measurement. However, the size of SiPMs are on the order of the pixel pitch (crystal size) and quantifying the differential uniformity is not feasible. However, the integral uniformity is an appropriate quantity to measure our gamma camera uniformity. This can be quantified extrinsically (with a collimator) or intrinsically (detector only) . Since we have not considered a collimator yet, we calculated the intrinsic integral uniformity of our gamma camera to be $\pm 3\,\%$ using eqn. 5.3. J. Halama noted that the integral uniformity should typically be within 2-3 % (Halama, 1987). This corrected image is what we expected, a uniform flood histogram and is within clinical gamma camera standards.

$$Integral\,uniformity = \pm\left(\frac{Max - Min}{Max + Min}\right) \times 100\% \tag{5.3}$$

Detector Limitations

The SiPM needs be operated sufficiently above breakdown to minimize the effect from charge collection time, and other effects such as carrier recombination and trapping to create a more uniform electric field across the detector (Knoll, 2000). On the same note, one should not impart too large a voltage as dark noise may increase. The dark count signal was measured as a function of bias voltage, but acquiring raw data from our gamma camera without any radioactive sources, besides background. As the bias voltage is increased, there is a higher contribution of thermally generated electron hole pairs and the electric field is also larger increasing the probability of triggering an avalanche. This results in a non-linear increase in dark counts as shown in fig. 5.10 as the bias voltage is increased. Therefore, operating the SiPM with too high a voltage may significantly deteriorate the gamma camera performance.

A Tc-99m source was used to analyze and determine an optimal operating voltage for the SiPM. The peak to valley ratio is a measurement to quantify the ability to discriminate the crystals. This is measured by averaging the peak number of counts divided by the baseline counts for each discrete crystal. The peak to valley ratio was measured at different bias voltages and compared to the energy resolutions at the corresponding bias voltage. The results of these measurements are shown in fig. 5.11. There is a significant amount of fluctuation in the peak to valley ratios and energy resolutions at bias voltages close to V_{bd}. However, as the bias voltage increases, the peak to valley ratio increases and the energy resolution improves. At the bias voltage

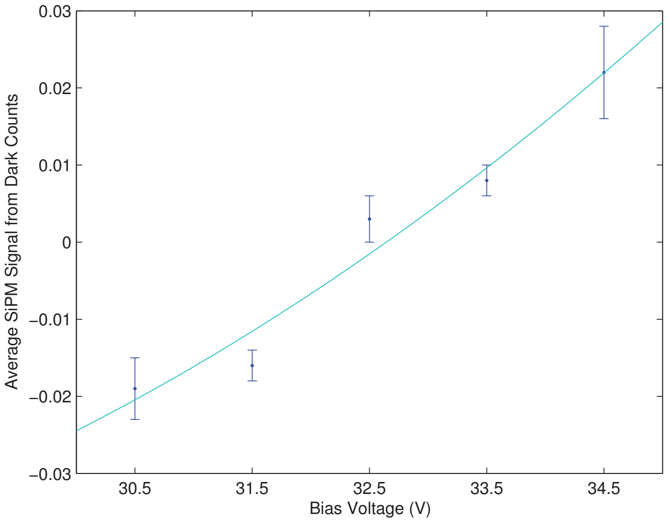

Figure 5.10: Dark signal variation versus bias voltage

increases beyond 31 V, the peak to valley ratio begins to decrease. As well, the energy resolution slowly decreases. There is an approximate optimal operating voltage which occurs approximately 2 V above breakdown. Therefore, the optimal operating voltage was determined to be $\sim 31\,V$. The decrease in the peak to valley ratio with increasing bias voltage is a result of a higher probability of thermally generated electron-hole pairs and cross talk between SiPM microcells. In addition the significant uncertainty in the energy resolution at bias voltages close to breakdown is influenced by a combination of the probability of cross talk and avalanche triggering probability.

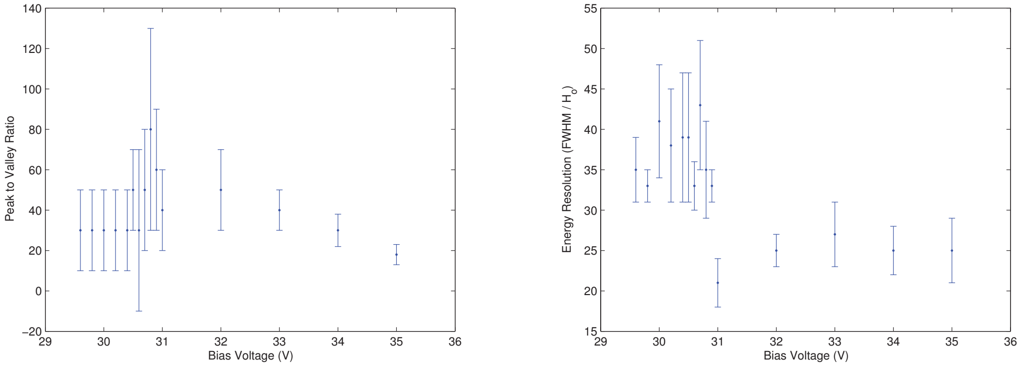

Figure 5.11: Peak to valley ratio of Tc-99m image versus bias voltage (left), Tc-99m energy resolution versus bias voltage (right)

Energy Resolution

There are several factors which limits our detector performance in regards to energy resolution. The potential factors which may affect the quality of the response function are external light contributions, thermally generated electron hole pairs, and the statistical noise arising from the detector nature of the signal itself and statistical noise limit on the detector performance (Knoll, 2000). The effects of statistical fluctuation in the number of counts would be less significant if there was a higher efficiency of photon detection. In addition, if there are a large number of photons near the number of pixels, the probability that a second photon is incident on the same microcell increases. Since the microcell is already in avalanche, the second photon is not detected, thereby limiting the accuracy of energy detection.

Dead Time

There are two dead time behaviours which are exhibited by radiation detectors. The first being a non-paralyzable model. In the case of the non paralyzable model, a fixed dead time exists in which events occurring during the dead time go undetected and ignored. Due to the detector dead time, we may observe a smaller number of counts than is actually incident on the detector. For the non-paralyzable case, with measured counting rate, m, the true interaction rate, n is given by eqn. 5.4 with τ equal to the system dead time (Knoll, 2000).

$$n = \frac{m}{1 - m\tau} \tag{5.4}$$

The second model is the paralyzable model. This dead time in this model is dependent on the counting rate. If a second event arrives during the dead time of the initial event, it acts as a new detected event and extends the dead time by τ. In this case, the dead time varies depending on how close or far apart events are detected. It is important to note that with the paralyzable model, the measured counting rate, m may correspond with two potential true counting rates. This is because as the count rate increases to very high levels, the detector experiences a longer dead time which may result in a count rate equivalent to that at lower count rates.

$$m = ne^{-n\tau} \tag{5.5}$$

The timing diagrams depicting these dead time behaviours are shown in the fig. 5.12 below:

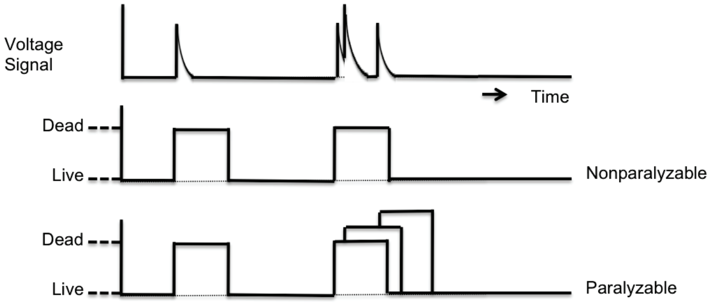

Figure 5.12: Paralyzable and nonparalyzable dead time models

The theoretical dead time of our detector system is approximately 25 μs which should yield a maximum count rate of $1/\tau = 40000\,cps$ (counts per second) using the non-paralyzable model. When an event is detected, the comparator is set as the trigger for our peak detection circuit. The DET and RST pin of the peak detect and hold chip go into peak detect mode for $\sim 8\,\mu s$. They are then sent into peak hold mode for analog to digital conversion for all 16 channels. Theoretically, the ADC conversion should take approximately 16 μs because the DAQ has a maximum clock rate of 1 MHz. However, this time may be a little bit longer because the DAQ itself requires time to respond to the trigger signal. The DET and RST pins are programmed such that the peak detect and hold mode consumes 25 μs of the pulse processing time during which time no other events can be detected.

We compared the measured counting rate as a function of the relative true counting rate at a bias voltage of 31.5V to determine the detector dead time which is seen in fig. 5.13. NEMA NU1 suggests the use of copper plates to adjust the count rate (NEMA Standards Publication, 2001). However, we simply moved the source with various distances from the detector to achieve different count rates. The measured dead time of the detector is 26 μs.

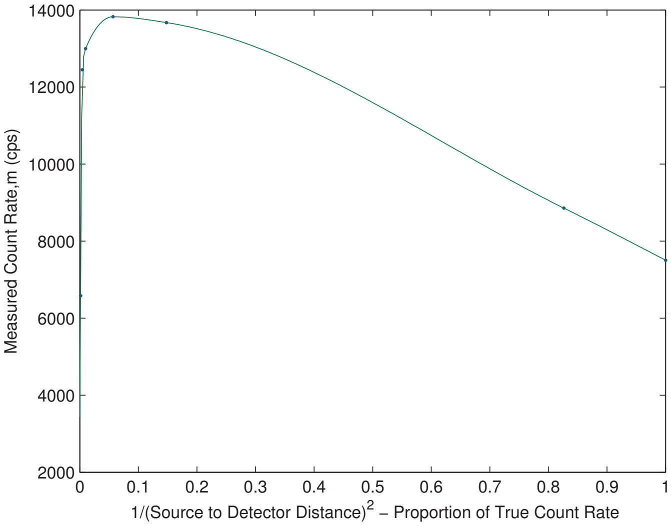

Figure 5.13: Variation of the observed count rate versus the true interaction rate

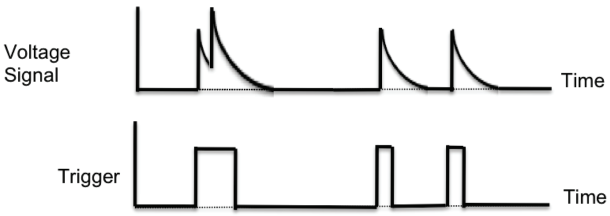

Figure 5.14: Timing diagram of comparator output

Our gamma camera system behaves like a paralyzable system because while the comparator is held high, pulse pile up may occur. Additional events may be triggered causing the comparator to remain high for an extended period of time. The length of the comparator output varies depending on the number of photons incident within any period of time. This is shown in the timing diagram in fig. 5.14. Since the peak detect mode occurs within the first $8\,\mu s$ of detection, the pulse pile events are not actually detected. However, because we get pulse pile up occurring during the trigger signal, our detector dead time is actually limited by this pulse pile up. Following the analog to digital conversion, data is stored in batches and then sent to the computer for further signal processing. This portion of the signal processing diminishes the ability to achieve higher count rates resulting in a dead time of $26\,\mu s$. If the digital signals were not transferred to the computer, the maximum count rate extends to $\sim 17000\,cps$ resulting in a dead time of $\sim 21\,\mu s$. In addition, as the bias voltage increases, the limiting measured count rate increases. However, this may not actually represent the true count rate, rather there is an increase in thermally generated counts and dark counts.

The cause for pulse pile up occurs at the comparator level and is a result of insufficient pulse shaping in the pulse processing electronics. This accounts for the discrepancy between the theoretical and the actual gamma camera dead time. The peak detect and hold circuit/DAQ requires $25\,\mu s$ to detect and digitize the signal. While the rise time of the pulse is fast (on the order of ns), the signal takes approximately $25\,\mu s$ to decay. During the decay portion of the signal, if another event is detected, the signal 'piles up' on the previous pulse resulting in the comparator to remain high. This is shown in fig. 5.14. The length of the comparator pulse limits the count rate because a new event cannot be detected until the comparator is reset. If a pulse shaper was implemented, the signal would be shaped into a Gaussian pulse truncating the long tail allowing another event to be detected. The comparator would then be able to distinguish between the two events and the pulse height analyzers or peak detection circuits can accurately quantify the maximum signal. A pulse shaping component will be one of the future improvements to our gamma camera. So while, our gamma camera produced a dead time on the order of what we expected. We limit our true counting rate to $1/\tau$ due to the paralyzable nature of our detector

Another factor to consider is the uniformity of the detector. From the previous section, we quantified the integral uniformity of our gamma camera with a uniformity correction map. This correction map assigns a scaling factor to each crystal. The measured count rate ($cps_{measured}$) can be corrected to the true count rate (cps_{true}) by multiplying the measured count rate by scaling factors (γ) for each crystal as shown in eq. 5.6.

$$cps_{true} = cps_{measured} \sum_{i=1:N}^{N} \frac{\gamma_i}{N} \tag{5.6}$$

We calculated a 2.8 correction factor resulting in an expected true count rate of $\approx$ 48000 cps. Since our gamma camera has a theoretical dead time of $25\mu s$, even if we were able to detect the true count rate, we would still not be able to detect all counts as the limiting count rate is 40000cps. With that said, the paralyzable response of our system limits the maximum true count rates ($1/\tau$) we can detect which in turn limits the measured count rate ($1/e\tau$).

System Sensitivity

The relative detector sensitivity was measured in conjunction with determining the detector dead time. The absolute detection efficiency is given by the eqn. 5.7. However this is not necessarily the optimal way of reporting the efficiency since it does not account for the solid angle in which photons emitted from the source are actually incident on the detector. As well, it also doesn't account for the dead space regions on the detector. Another parameter used to describe the efficiency is the intrinsic efficiency (eqn. 5.8) which takes into account the distance from the source to detector distance, dead space, energy and detector material (Knoll, 2000).

$$\epsilon_{abs} = \frac{number\ of\ counts\ recorded}{number\ of\ radiation\ events\ emitted\ by\ the\ source} \tag{5.7}$$

$$\epsilon_{int} = \frac{number\ of\ counts\ recorded}{number\ of\ radiation\ events\ incident\ on\ the\ detector} \tag{5.8}$$

Bear in mind that the overall sensitivity of the system may decrease with the addition of a collimator. The sensitivity of the detector itself is related to our dead time measurement. The system sensitivity is limited due to the current increase in dead time. Further work will include quantifying the gamma camera sensitivity. Typically, quality measurements for gamma camera sensitivity is dependent on a few factors such as collimator type, gamma ray energy, and source position/configuration etc. Without actual measurements we can conclude the system sensitivity of our gamma camera without the collimator and other factors need to be improved such that reasonable sensitivity measurements can be achieved when all other factors are considered (NEMA Standards Publication, 2001). The detector sensitivity is usually reported in (cps)/MBq. Typical sensitivity contributions of collimators can range from $(0.28 - 0.58) \times 10^6\, cps/MBq$ (Halama, 1987).

Six

Conclusion

In this thesis, we have investigated a novel gamma camera based on silicon photomultipliers in place of traditional photomultiplier tubes.

Simulation exercises were used to evaluate various scintillator geometries in order to optimize image resolution and energy resolutions. Based on these results, we have designed and built a prototype detector using a 4 × 4 array of SiPMs.

Silicon photomultipliers have been shown to potentially become a new standard in gamma cameras. They perform well in magnetic fields and the magnetic field has no effect on the accompanying electronics. The measured energy resolution of a Co-57 source was $35 \pm 3\,\%$ in the absence of a magnetic and $33 \pm 3\,\%$ within the presence of a $130\,\mathrm{mT}$ magnet. The gamma camera will be tested in larger magnetic fields, on the order of MRI magnetic field strengths. Higher bias voltage results in energy resolution degradation. However, while the intrinsic spatial resolution is limited, the measured spatial resolution before corrections improves with increasing bias voltage. This aids in improving crystal identification through image segmentation. We were able to obtain an energy resolution of $\sim 28 - 30\,\%$ with Tc-99m, and $\sim 11 - 13\,\%$ with Na-22.

The image was reconstructed using the centroid method to position the detected events. Currently all SiPM signals are being read out for positioning. It is known positioning through Anger logic results in an edge compressed image distortion. The current imaging system consists of a 16 channel readout and if the imaging system is to be expanded to a larger area detector, it may become cumbersome to process data from all contributing SiPMs. To minimize the number of readout channels, Chaudhari et al proposed a positioning algorithm called the Adaptive method which incorporates Anger logic and Zhang's method to produce a relatively non-distorted image (Chaudhari et al., 2009). This method only requires a total of four readout signals compared to potentially hundreds of readout channels and could be implemented in the future to minimize computational demand. The form factor of the SensL SiPM allows for tiling multiple SiPM arrays together, so the gamma camera can be expanded into a larger area detector. A novel multiplexing scheme will also be investigated which would require 32 channels versus 256 readout channels.

Further development in the gamma camera design and characterization can be explored. Investigation into collimator material for magnetic field compatibility and geometry can be explored for optimal performance. As well, the gamma camera performance can be optimized by the addition of a pulse shaping component which in turn would improve the detector efficiency.

Bibliography

Abramowitz, M. and M. Davidson (2010). Concepts in digital imaging technology - photomultiplier tubes.

Ahmed, S. (2007). *Physics and Engineering of Radiation Detection*. Amsterdam, The Netherlands: Elsevier Academic Press.

Alva-Sanchez, H., T. Murrieta, E. Moreno-Barbosa, M. Brendan, C. Ruiz-Trejo, A. Martinez-Davalos, and M. Rodriguez-Villafuerte (2010, February). A small-animal PET system based on LYSO crystal arrays, PS-PMTs and a PCI DAQ board. *IEEE Transactions on Nuclear Science 57*(1), 85–93.

Analog Devices (2001). *Peak Detect with Reset and Hold Mode*. Norwood, MA: Analog Devices.

Analog Devices (2003). *250MHz, General Purpose Voltage Feedback Op Amps AD8047/8048*. Analog Devices.

Aull, B., A. Loomis, D. Young, R. Heinrichs, B. Felton, P. Daniels, and D. Landers (2002). Geiger-mode avalanche photodiodes for three-dimensional imaging. *Lincoln Laboratory Journal 13*(2), 335–350.

Barbosa, F., H. Dong, B. Kross, S. Lee, Y. Mack, J. McKisson, A. Weisenberger, W. Xi, C. Zorn, S. Majewsk, A. Stolin, C. Howell, A. Crowell, C. Reis, and M. Smith (2010). Development of a mini-PET detector baased on silicon photomultiplier arrays for plant imaging applications. In *IEEE NSS/MIC Conference*.

Barral, J. (2004). *Study of Silicon Photomultipliers*. Ph. D. thesis, Max Planck Institut fur Physik and Ecole Polytechnique.

Breton, E., P. Choquet, C. Goetz, J. Kintz, P. Erbs, R. Rooke, and A. Constantinesco (2007). Dual SPECT/MR imaging in small animal. *Nuclear Instruments and Methods in Physics Research A 571*, 447–448.

Britvitch, I., E. Lorenz, A. Olshevski, D. Renker, Z. Sadygov, R. Scheuermann, A. Stoykov, A. Werner, and I. Zheleznykh (2007). Development of scintillation detectors based on avalanche microchannel photodiodes. *Nuclear Instruments and Methods in Physics Research A 571*, 317–320.

Buxton, R. (2009). *Introduction to Functional Magnetic Resonance Imaging* (2 ed.). Cambridge University Press.

Buzhan, P., B. Dolgoshein, L. Filatov, A. Ilyin, V. Kaplin, A. Karakash, S. Klemin, R. Mirzoyan, A. Otte, E. Popova, V. Sosnovtsev, and M. Teshima (2006). Large area silicon photomultipliers: Performance and applications. *Nuclear Instruments and Methods in Physics Research A 567*(1), 78–82.

Buzhan, P., B. Dolgoshein, A. Ilyin, B. Kantserov, V. Kaplin, A. Karakash, A. Pleshko, E. Popova, S. Smirnov, and Y. Volkov (2001). An advanced study of silicon photomultiplier. In *ICFA Instrumentation Bulletin*.

Chaudhari, A., A. Joshi, Y. Wu, R. Leahy, S. Cherry, and R. Badawi (2009). Spatial distortion correction and crystal identification for MRI-compatible position-sensitive avalanche photodiode-based PET scanners. *IEEE Transactions on Nuclear Science 56*(3), 549 – 556.

Cherry, S., J. Sorensen, and M. Phelps (2003). *Physics in Nuclear Medicine* (3 ed.). Philadelphia, Pennsylvania: Saunders.

Collazuol, G. (2008). Review of silicon photo-multiplier physics and applications, including a study at low temperature. Innovative Particle and Radiation Detectors.

Denk, W., J. Strickler, and W. Webb (1990). Two-photon laser scanning fluorescence microscopy. *Science 248*, 73–76.

Efthimiou, N., G. Argyropoulos, G. Panayiotakis, M. Georgiou, and G. Loudos (2010). Initial results on SiPM performance for use in medical imaging. In *IEEE International Conference on Imaging Systems and Techniques.*

Elad, M. (2002, May). Algorithms for noise removal and the bilateral filter. Scientific Computing and Computational Mathematics (SCCM) Program - Stanford University.

Elmore, J., M. Barton, V. Moceri, S. Polk, P. Arena, and S. Fletcher (1998). Ten-year risk of false positive screening mammograms and clinical breast examinations. *The New England Journal of Medicine 338*(16), 1089–1096.

Espana, S., G. Tapia, L. Fraile, J. Herraiz, E. Vicente, J. Udias, M. Desco, and J. Vaquero (2008). Performance evaluation of SiPM detectors for PET imaging in the presence of magnetic fields. In *IEEE Nuclear Science Symposium Conference Record*.

Fortin, P. (2000). An instrument for studying the response of STACEE camera components to different lighting conditions. Master's thesis, McGill University.

Gonzalez, R. and R. Woods (2008). *Digital Image Processing*. Upper Saddle River, New Jersey: Pearson Prentice Hall.

Goscin, C., C. Berman, and R. Clark (2001). Magnetic resonance imaging of the breast: Sensitivity and specificity. *Cancer Control 8*(5), 399–406.

Grigorieve, E., A. Akindinov, M. Breitenmoser, S. Buono, E. Charbon, C. Niclass, I. Desforges, and R. Rocca (2007). Silicon photomultipliers and their bio-medical applications. *Nuclear Instruments and Methods in Physics Research A 571*, 130–133.

Gruber, G., W. Moses, S. Derenzo, N. Wang, E. Beuville, and M. Ho (1998). A discrete scintillation camera module using silicon photodiode readout of CsI(Tl) crystals for breast cancer imaging. *IEEE Transactions on Nuclear Science 45*(3), 1063–1068.

Halama, J. (1987). *Quality Assurance in Gamma Camera and SPECT*. Loyola University Medical Center.

Hamamatsu (2007). *Photomultiplier Tubes* (3a ed.). Hamamatsu.

Hamamura, M., S. Ha, W. Roeck, L. Muftuler, D. Wagenaar, D. Meier, B. Patt, and O. Nalcioglu (2010). Development of an MR-compatible SPECT system (MRSPECT) for simulataneous data acquisition. *Physics in Medicine and Biology 55*, 1563–1575.

Hawkes, R., A. Lucas, J. Stevick, G. LLosa, S. Marcatili, C. Piemonte, A. Del Guerra, and T. Carpenter (2007). Silicon photomultiplier performance tests in magnetic resonance pulsed fields. In *IEEE Nuclear Science Symposium Conference Record*, pp. 3400–3403.

Herbert, D., S. Moehrs, N. D'Ascenzo, N. Belcari, A. Del Guerra, F. Morsani, and V. Saveliev (2007). The silicon photomultiplier for application to high-resolution positron emission tomography. *Nuclear Instruments and Methods in Physics Research A 39*(4), 84–87.

Huda, W., B. Lentle, and J. Sutherland (1989). The effective dose equivalent in radiology. *Canadian Association of Radiologists Journal 40*, 254–263.

Iniewski, K. (2010). *Semiconductor Radiation Detector Systems.* CRC Press.

Jackson, J., D. Phelan, A. Morrison, R. Redfern, and A. Mathewson (2002). Characterization of geiger mode avalanche photodiodes for fluorescence decay measurements. In *Proceedings of SPIE*, Volume 4650-07.

Jahne, B. (2005). *Digital Image Processing* (6 ed.), Volume 1. Springer.

Jørgensen, J. (2011). Scanning probe image processor - watershed segmentation.

Kal, S. (2002). *Basic Electronics Devices Circuits And IT Fundamentals.* Prentice Hall of India.

Knoll, G. (2000). *Radiation Detection and Measurement* (3 ed.). Ann Arbour, Michigan: John Wiley and Sons, Inc.

Kovaltchouk, V., G. Lolos, Z. Papandreou, and K. Wolbaum (2005). Comparison of a silicon photomultiplier to a traditional vacuum photomultiplier. *Nuclear Instruments and Methods in Physics Research A 538*(1-3), 408–415.

Llosa, G., N. Belcari, M. Bisogni, G. Collazuol, S. Marcatili, S. Moehrs, F. Morsani, C. Piemonte, and A. Del Guerra (2009). Energy and timing resolution studies with silicon photomultipliers (SiPMs) and 4-pixel SiPM matrices for PET. *IEEE Transactions on Nuclear Science 56*(3), 543–548.

Majewski, S., J. Proffitt, J. McKisson, R. Raylman, A. Stolin, and A. Weisenberger (2008). Initial tests of a compact imaging photomultiplier made from array of 3x3mm hamamatsu MPPC-SMD modules.

McClish, M., P. Dokhale, J. Christian, C. Stapels, and K. Shah (2007). Characterization and scintillation studies of a solid-state photomultiplier. *Nuclear Instruments and Methods in Physics Research A 572*, 1065–1070.

McElroy, D., V. Saveliev, A. Reznik, and J. Rowlands (2007). Evaluation of silicon photomultipliers: A promising new detector for MR compatible PET. *Nuclear Instruments and Methods in Physics Research A 571*, 106–109.

Moser, H. (2006). Silicon photomultipliers, a new device for low light level photon detection. In *American Institute of Physics Conference Proceedings*.

Mulero, F., F. Nicolas, M. Castellon, T. Fuentes, P. de la Cruz, V. Roca, L. Abad, and J. Nuno de la Rosa (2000). 99m Tc-MIBI scintigraphy compared to mammography in the diagnosis of breast cancer in dense , operated and young women breasts. *Revista Espanola de Medicina Nuclear 19*(5), 344–349.

NCHPS (2011). *Nuclide Safety Data Sheet - Co57*. North Carolina Health Physics Society.

NCRP (1989). *Exposure of the U.S. Population from Diagnostic Medical Radiation*. National Council on Radiation Protection and Measurements.

NEMA Standards Publication (2001). *NEMA NU1 Performance Measurements of Scintillation Cameras*. National Electrical Manufacturers Association.

Paris, S. (2007). Fixing the Gaussian blur: The bilateral filter. *MIT Computer Science and Artificial Intelligence Laboratory*.

Perkin Elmer (1999). *Indium-111 Handling Precautions*. 549 Albany St, Boston, MA: Perkin Elmer Life Sciences.

Perkin Elmer (2003). *Avalanche Photodiodes: A User's Guide*. Perkin Elmer.

Safety, O. and E. Health (2010). *Radionuclide Safety Data Sheets - Technetium-99m*. University of Michigan.

Saint-Gobain Crystals (2007). *CsI(Tl), CsI(Na) - Cesium Iodide - Scintillation Material*. Saint-Gobain Crystals.

Schaart, D., H. T. van Dam, S. Seifert, R. Vinke, P. Dendooven, H. Lohner, and F. Beekman (2009). A novel, SiPM-array-based, monolithic scintillator detector for PET. *Physics in Medicine and Biology 54*(11), 3501–3512.

Schotanus, P., R. Kamermans, and P. Dorenbos (1990, April). Scintillation characteristics of pure and Tl-doped CsI crystals. *IEEE Transactions on Nuclear Science 37*(2), 177–182.

Semwogerere, D. and E. Weeks (2005). *Encyclopedia of Biomaterials and Biomedical Engineering: Confocal Microscopy*. Taylor and Francis.

SensL (2009, November). *SensL - SPM Array4 Four Side Tileable Large Area SPM Detector and SPMArray4 Pre-amplification 16 channel Readout Electronics*. Riverview Business Park, Blackrock, Cork, Ireland: SensL.

SensL (2010a). *ArraySL-4 Scalable Silicon Photomultiplier Array Datasheet*. SensL.

SensL (2010b). *Silicon Photomultiplier for Simulataneous PET-MRI*. SensL.

SensL (2010c). *Silicon Photomultipliers for Radiation Detection Applications*. SensL.

SensL (2010d). *SPMArray4 - Scalable Silicon Photomultiplier Array*. SensL.

SensL (2010e). *SPMMatrix 16x16 SPM Readout Circuit Interface Guide*. Blackrock, Cork, Ireland: SensL.

Serway, R. and J. Jewett (2004). *Physics for Scientists and Engineers with Modern Physics: Volume 2*. Brooks Cole - Thomson Learning.

Smith, J. (2007). Design and construction of an avalanche photodiode-based gamma camera prototype. Master's thesis, McMaster University.

So, P., C. Dong, B. Masters, and K. Berland (2000). Two-photon excitation fluorescence microscopy. *Annual Review of Biomedical Engineering 02*, 399–429.

Spieler, H. (2001). Radiation detectors and signal processing. Signal Formation and Detection Thresholds.

Stapels, C., W. Lawrence, and J. Christian (2006). CMOS solid-state photomultiplier for detecting scintillation light in harsh environments. In *SNIC Symposium*.

Tomasi, C. and R. Manduchi (1998). Bilateral filtering for gray and color images. In *Proceedings of the 1998 IEEE International Conference on Computer Vision*.

Wagenaar, D., M. Kapusta, J. Li, and B. Patt (2006, August). Rationale for the combination of nuclear medicine with magnetic resonance for pre-clinical imaging. *Technology in Cancer Research and Treatment 5*(4), 343–350.

Wernick, M. and J. Aarsvold (2004). *Emission Tomography: The Fundamentals of PET and SPECT.* Elsevier Academic Press.

Yokoyama, M., T. Nobuhara, M. Taguchi, T. Nakaya, T. Murakami, T. Nakadaira, K. Yoshimura, K. Kawagoe, Y. Tamura, T. Iijma, Y. Mazuka, K. Miyabayashi, S. Iba, H. Miyata, and T. Takeshita (2006). Development of multi-pixel photon counters. In *SNIC Symposium*, pp. 1–6.

Zhang, M. (2009). Bilateral filter in image processing. Master's thesis, Louisiana State University.